

Magnetic Cluster Formation in Al_2O_3

Vanthini Nelson Adoons

(200003943)

A dissertation submitted in fulfillment of the academic requirements for the
degree of Master of Science

School of Chemistry and Physics
College of Agriculture, Engineering, and Science
University of KwaZulu-Natal, Westville Campus
Durban

August 2017

Preface

The research contained in this dissertation was completed by the candidate while based in the Discipline of Physics, School of Chemistry and Physics, College of Agriculture, Engineering and Science, University of KwaZulu-Natal, Westville Campus.

The contents of this work have not been submitted in any form to another university, and except where the work of others is acknowledged in the text, the results reported are due to investigations by the candidate.

Signed: Dr. Mathew K. Moodley (Supervisor)

Date:

A handwritten signature in black ink, appearing to read 'M. Moodley', is written over a horizontal line.


Signed: VN Adoons (Student)

Date: 18/08/17

Declaration

I, Vanthini Nelson Adoons, declare that:

- (i) The research reported in this dissertation, except where otherwise indicated, is my original work;
- (ii) This dissertation has not been submitted for any degree or examination at any other university;
- (iii) This dissertation does not contain other persons' data, pictures, graphs or other information unless specifically acknowledged as being sourced from other persons;
- (iv) This dissertation does not contain other persons' writing unless specifically acknowledged as being sourced from other researchers. Where other written sources have been quoted, then:
 - a) their words have been re-written but the general information attributed to them has been referenced;
 - b) where their exact words have been used, their writing has been placed inside quotation marks and referenced;
- (v) This dissertation does not contain text, graphics or tables copied and pasted from the Internet, unless specifically acknowledged, and the source being detailed in the dissertation and in the Reference section.



Signed: Vanthini N. Adoons

Date: 18/08/2017

In memory of my brother and sister:

Mthethozumeli A. Adoons & Nelisiwe H. Shandu

Acknowledgements

Finally, the work is done and now the only thing left is to put on record all I owe to so many people. I wish to recognise a number of people who have contributed greatly towards this work.

I am indebted to my supervisor *Dr. Mathew K. Moodley* and my co-supervisor *Professor Krishanlal Bharuth-Ram* for their assistance during my experimental work and data analysis. I would also like to express my sincere gratitude to them for reading drafts of my dissertation a number of times and providing me with useful suggestions and feedback. Further, thank you *Professor Krishanlal Bharuth-Ram* for your patience, invaluable expertise, critical comments made on this dissertation and many hours of consultation. Thank you so much. You have contributed immensely to my becoming a better research student.

My special appreciation goes to *Professor Terry B. Doyle* from iThemba LABS, for his insights and expertise during VSM measurements and *Dr. Hilary Masenda* for his assistance during CEMS data analysis.

Most of all I would like to thank my father (*Msithi*), mother (*Adelaide*) and my sisters (*Nonzwakazi and Nompiliso*) for their support and encouragement throughout my studies. My thanks are also directed to my closest friends, *Dr. Remmy Musumpuka*, *Mr. Vusi Masondo*, *Mr. Siya Mhlongo* and *Mr. Zulpher Maropeng Hopane* for the encouragements during hard times.

Abstract

In this study, we search for the formation of magnetic clusters on Al_2O_3 implanted with ^{56}Fe and ^{57}Fe ions to a total fluence of $1.12 \times 10^{16} \text{ ions.cm}^{-2}$, corresponding to a concentration of approximately 4 at. %. The characterization methods include conversion electron Mössbauer spectroscopy (CEMS) and vibrating sample magnetometer (VSM).

CEMS measurements were carried out on the as-implanted sample and after annealing the sample up to 1173 K in air. The CEMS spectrum in the ‘as-implanted’ state is in good agreement with earlier studies and show that the implanted iron ions are present in four charge state Fe^{4+} , Fe^{3+} , Fe^{2+} , and Fe^0 . Annealing at temperatures above 873 K resulted in significant changes in the spectra. The dominant spectral components were two quadrupole split doublets with isomer shifts of 0.36(3) and 0.33(2) mm/s which are characteristic of Fe^{3+} .

Annealing at higher temperatures (up to 1173 K), showed a decrease in the quadrupole splittings of the doublets, indicating an increase in the size of the clusters. The absence of ferromagnetic sextets in the CEMS spectra indicate that the clusters are nanometer in size and display superparamagnetic behavior. Magnetization curves of the sample at $T = 4 \text{ K}$ and room temperature after annealing at 1173 K, confirm the superparamagnetic behavior of the clusters at room temperature.

Nomenclature

EFG	Electric Field Gradient
$(V_{zz})_{Lat}$	Lattice contributions to the EFG
$(V_{zz})_{Val}$	Valence electron contributions to the EFG
$\langle x^2 \rangle$	Mean square displacement
$ \psi(0) ^2$	Probability density
ΔE_Q	Quadrupole splitting
δ	Isomer shift
\vec{B}_{hf}	Hyperfine magnetic field
\vec{B}_{loc}	Local magnetic field
CEMS	Conversion electron Mössbauer spectroscopy
E_o	Transition Energy
E_R	Recoil Energy
E_γ	Gamma-ray energy
f	Recoil-free fraction
Fe	Iron
FWHM (Γ)	Full width of spectral line at half maximum height
Al_2O_3	Aluminium Oxide
k_B	Boltzmann Constant
m	Mass
M	Lattice mass

T	Temperature
$t_{1/2}$	Half-life of radioactive nucleus
RT	Room Temperature
LABS	Laboratory for Accelerated-Based Sciences
VSM	vibrating sample magnetometer
K	Kelvin scale
eMS	emission Mössbauer spectroscopy
σ	Gaussian broadening
XPS	X-ray photoelectron spectroscopy
f_A	Areal fraction
EC	Electron capture
T_A	Annealing temperature
MCA	Multi - channel Analyser
PHA	Pulse Height Analyser
TMS	Transmission Mössbauer Spectroscopy
MCS	Multi – channel scaling
UKZN	University of KwaZulu-Natal
DUT	Durban University of Technology
nm	nanometers
M_s	Saturation moment
M	moment
B	applied field
TRIM	Transport of ions in matter

HV	High voltage
MDU	Mössbauer drive unit
FG	Function Generator
μ	Magnetic moment of the particle/cluster
eV	electron volts
μm	micrometer
PPMS	Physical Properties Measurement System
mm/s	millimetres per second
cm	centimeter

Table of Contents

Preface	i
Declaration	ii
Acknowledgements	iv
Abstract	v
Nomenclature	vi
List of Figures	xii
List of Tables	xv
CHAPTER 1.....	1
Fundamental Concepts and Literature Review	1
1.1 Properties of Alumina (α -Al ₂ O ₃)	2
1.2 Point defects in a crystal.....	4
1.3 Literature review of Mössbauer studies in Al ₂ O ₃	5
1.4 Aims and objectives of this study	6
1.5 Dissertation Outline	7
CHAPTER 2.....	8
Mössbauer Effect and Hyperfine Interactions.....	8
2.1 The Mössbauer Effect.....	9
2.2 Recoil free fraction.....	11
2.3 Spectral line shape and Natural linewidth	14
2.4 Mössbauer isotope: ⁵⁷ Fe	16

2.5	Mössbauer spectrum.....	17
2.6	Hyperfine interaction parameters	18
2.6.1	Electric monopole interaction: Isomer shift (δ)	18
2.6.2	Electric quadrupole interaction: Quadrupole splitting (ΔE_Q).....	21
2.6.3	Magnetic dipole interaction: Magnetic splitting	24
2.6.4	Combined magnetic and quadrupole interactions.....	26
2.6.5	Angular dependence of hyperfine parameters	28
2.6.5.1	Quadrupole splitting	28
2.6.5.2	Magnetic splitting	29
CHAPTER 3.....		31
Experimental Details		31
3.1	Introduction.....	31
3.2	Sample Preparation	31
3.2.1	Implantation Parameters, and Profiles.....	32
3.3	Mössbauer spectroscopy.....	35
3.3.1	Conversion Electron Mössbauer Spectroscopy (CEMS)	35
3.3.2	CEMS Measurements and Annealing Conditions.....	37
3.3.3	CEMS Detector	38
3.3.4	Procedure of operation in CEMS.....	39
3.3.5	Data acquisition Electronics	43
3.3.6	Calibration of Mössbauer spectra.....	44
3.4.7	Data analysis.....	46

3.5	Vibrating Sample Magnetometry (VSM)	47
3.5.1	Principle of Operation.....	47
3.5.2	VSM measurements.....	49
CHAPTER 4	50
Analysis, Results, and Discussion.....		50
4.1	CEMS Measurements on Fe-implanted Al₂O₃.....	50
4.1.1	Analysis and Results.....	50
4.1.2	Spectral parameters and Assignments	54
4.2	VSM Studies	56
4.3	Summary of ⁵⁷Fe/⁵⁶Fe implanted in Al₂O₃ results.....	59
CHAPTER 5	60
Concluding Remarks.....		60
References.....		61

List of Figures

Figure 1.1: (a) Corundum structure in α -Al ₂ O ₃ , (b) top view of the corundum structure, (c) octahedral structure of α -Al ₂ O ₃	2
Figure 1.2: A schematic illustration of different types of point defects.....	5
Figure 2.1: Momentum P_n and recoil energy E_R lost by a free nucleus upon γ -ray emission.....	9
Figure 2.2: Lack of resonant γ -ray absorption due to recoil energy lost to the emitting nucleus.....	10
Figure 2.3: Resonant emission and absorption of γ -ray.....	10
Figure 2.4: Intensity $I(E)$ plotted against transition energy E	14
Figure 2.5: Nuclear decay scheme of $^{57}\text{Co}^*$	16
Figure 2.6: Development of a Mössbauer spectrum.....	17
Figure 2.7: Effects of electric monopole interaction: isomer shift.....	19
Figure 2.8: Typical isomer shift values in iron compounds.....	20
Figure 2.9: Quadrupole splitting of ^{57}Fe and the resulting Mössbauer spectrum.....	23
Figure 2.10: Magnetic splitting of $I = 1/2$ and $I = 3/2$ states of ^{57}Fe and the corresponding sextet observed in a typical spectrum.....	26
Figure 2.11: Isomer shift δ and quadrupole splitting ΔE_Q , a) when only the magnetic dipole interaction is present and b) when the magnetic dipole interaction is perturbed by a small electric quadrupole interaction.....	27

Figure 3.1: Plot of concentration distribution of implanted Fe in Al ₂ O ₃ estimated from TRIM simulations.....	33
Figure 3.2: Ion ranges distribution profile for 50 keV of (a) ⁵⁶ Fe and (b) ⁵⁷ Fe implanted Al ₂ O ₃ at 7 ⁰	34
Figure 3.3: Damage profile for 50 keV of (a) ⁵⁶ Fe and (b) ⁵⁷ Fe implanted Al ₂ O ₃ at 7 ⁰	34
Figure 3.4: The nuclear decay scheme for ⁵⁷ Co and various electron emission processes for ⁵⁷ Fe that can follow resonance absorption of an incident 14.4 keV γ -photon.....	36
Figure 3.5: CEMS set-up at iThemba LABS.....	37
Figure 3.6: Schematic diagram of PPAD with a source of γ -ray.....	38
Figure 3.7: PPAD open and closed systems.....	39
Figure 3.8: Sample mounted on PPAD.....	40
Figure 3.9: PPAD mounted to a tank.....	41
Figure 3.10: Vacuum pump station at iThemba LABS Mössbauer Lab.....	42
Figure 3.11: Electronics and experimental set-up for CEMS.....	43
Figure 3.12: Triangular velocity profile as a function of channel number.....	45
Figure 3.13: Unfolded CEM spectrum corresponding to α -Fe foil.....	46
Figure 3.14: Folded Mössbauer spectra for α -Fe spectrum for Transmission MS (left) and Conversion electron MS measurements (right).....	46
Figure 3.15: Schematic representation of a VSM apparatus.....	48

Figure 4.1: CEM spectra of Fe-implanted Al_2O_3 collected after annealing at the temperatures shown.....	52
Figure 4.2: Area fraction of spectral components as a function of annealing temperature.....	55
Figure 4.3: Magnetization curves of $\text{Al}_2\text{O}_3\text{:}^{57}\text{Fe} + ^{56}\text{Fe}$ measured at 293 K and 4 K after annealing at 1173 K.....	57
Figure 4.4: The moment m normalized to the saturation moment m_s plotted as a function of B/T where B is the applied field and T the temperature.....	59

List of Tables

Table 1.1: Selected properties of α -Al ₂ O ₃	3
Table 2.1: Transition probabilities for the quadrupole split doublet in Mössbauer spectrum.....	29
Table 2.2: Angular distribution of the relative intensities for the magnetic sextet in ⁵⁷ Fe.....	29
Table 3.1: Implantation energy and fluences of iron species implanted in Al ₂ O ₃	33
Table 3.2: TRIM simulations of projected range and straggle for Al ₂ O ₃ implanted with ⁵⁶ Fe and ⁵⁷ Fe ions.....	35
Table 4.1: Extracted hyperfine parameters, isomer shift (δ), quadrupole splitting (ΔE_Q), area fraction (f_A) and Gaussian broadening (σ) as well as their assignments for all components required to fit the CEM spectra.	53

CHAPTER 1

Fundamental Concepts and Literature Review

Aluminium oxide, otherwise known as alumina, has the chemical formula Al_2O_3 . It is one of the most widely studied and used materials in the world. Aluminium oxide comes in several forms, *corundum* ($\alpha\text{-Al}_2\text{O}_3$), *diaspore* ($\text{Al}_2\text{O}_3 \bullet \text{H}_2\text{O}$), *gibbsite* ($\text{Al}_2\text{O}_3 \bullet 3\text{H}_2\text{O}$) and *bauxite* [1]. *Corundum* (or $\alpha\text{-Al}_2\text{O}_3$) is the most common and the only alumina phase stable at all temperatures [2, 3]. Other known forms of metastable aluminas are γ , η , θ , κ , χ polymorphs [2]. Due to differences in crystal structures, alumina may come in different forms. For example, $\alpha\text{-Al}_2\text{O}_3$ has a trigonal crystal structure while $\gamma\text{-Al}_2\text{O}_3$ has a cubic structure [4]. Due to its favorable mechanical, electrical, and thermal properties, aluminium oxide may be employed as a catalyst, in electronic substrates, in gas purification, as furnace linings, and as abrasives for grinding and milling. Its low density, high elastic properties, and high hardness make it a “good” candidate for high strain-rate situations [5].

In this chapter, a discussion of relevant properties of alumina is presented. In this study, aluminium oxide, or alumina, refers to commercially acquired single crystals Al_2O_3 used for research, industrial or structural applications. In addition, discussion of different types of point defects is included since their nature and lattice location is vital for the understanding of new properties in doped semiconductor materials. A literature review will examine details related to transition metals in oxides and in particular Mössbauer spectroscopy measurements in alumina. The aims and specific objectives of the project undertaken in this study are briefly explained, and an outline of the dissertation is given at the end of this chapter.

1.1 Properties of Alumina (α -Al₂O₃)

The crystal structure of α -Al₂O₃ consists of close planes (A and B planes) of large oxygen anions stacked in the sequence as illustrated in Figure 1.1 [6]. The crystal lattice of α -Al₂O₃ is formed from Al³⁺ (valence of +3) and O²⁻ (valence of -2) ions. To maintain neutrality, there can be only two Al³⁺ ions for every three O²⁻ ions in a unit cell. The aluminium cations occupy two-thirds of the octahedral sites, and oxygen anions occupy one-third of the octahedral sites [1, 7].

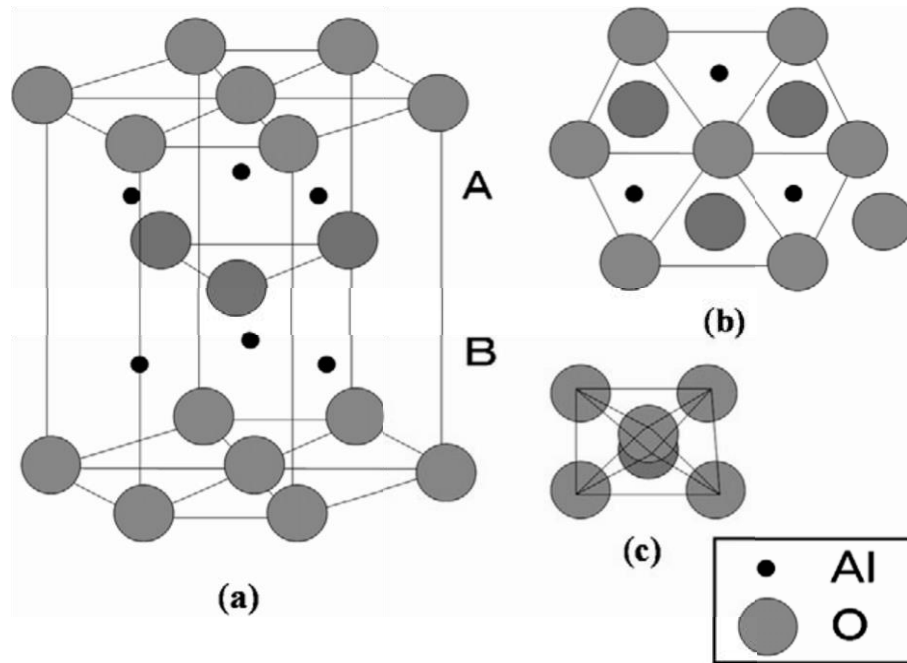


Figure 1.1: (a) Corundum structure in α -Al₂O₃, (b) top view of the corundum structure, (c) octahedral structure of α -Al₂O₃ [7].

Knowing the electrical, thermal and mechanical properties of the material of choice can lead to a better understanding of how the material can be used. Table 1.1 shows some selected properties for α -Al₂O₃ measured at room temperature.

Table 1.1: Selected properties for α -Al₂O₃.

Property	Value
Density (g. cm ⁻³)	3.98 [8]
Melting Point (°C)	2050 [9]
Tensile Strength (MPa)	300 - 900 [10]
Debye Temperature (K)	~ 900 [9]
Bond length (mean) (Å)	191[11, 12]
Band Gap (eV)	8.8 [13]

Alumina is a very hard material, diamond and few other synthetic substances such as *carborundum* and *silicon carbide* exceed its hardness. This property makes it to used as abrasive material. Its high melting point, i.e. 2050 °C [9], makes it a useful refractory and linings of special furnaces [1]. But other impurities and alloy elements form secondary phases that can melt at considerably lower temperatures. Certain surfaces of alumina have shown a strong conductive behavior (such as the $(\bar{1}10)$ surface [14], but in general, alumina is a strong electrical insulator with a very wide band gap [13, 14]. Its high volume resistivity of $> 10^{14}$ Ω .cm, and strong dielectric strength of 16.9 volts/mil [15] makes it an excellent insulator. The dielectric strength tends to dictate the amount of electric field strength the material can withstand before experiencing a breakdown of its insulating properties [15]. The strong electrical insulation behavior of alumina makes it a difficult material to examine under an electron microscope because the electron charge tends to build upon the surface [14]. A thin layer metal coating on alumina samples is required to make it possible to examine alumina under an electron microscope.

1.2 Point defects in a crystal

Point defects are imperfect point-like regions in a crystal structure. These defects can be distinguished as *intrinsic defects*, which occur in pure materials or *extrinsic defects*, which are due to impurity atoms. An *intrinsic defect* are classified a *vacancy defect*, which is due to a missing atom in a crystal lattice site and an *interstitial defect* is where an atom occupies an interstitial site (space between the atoms of the host material) where no atom would normally be present.

The *extrinsic point defects* are foreign atoms, which are referred to as *solutes* or *impurities*. These foreign atoms may be located in a lattice sites, forming a *substitutional impurities* (or *solutes*). They may also be located in interstitial sites, forming *interstitial impurities* (or *solutes*). However, if they are embedded in defect complexes in the lattice, they are referred to as *interstitial-vacancy* or *substitutional-vacancy* complexes. A *self-interstitial defect* is an extra atom that has crowded its way into an interstitial void in the crystal structure. *Self-interstitial defects*, occurs in low concentrations in metals because they distort and highly stress the tightly packed lattice structure. The different types of point defects are shown in Figure 1.2.

To alter the electrical and optical properties of semiconductors, controlled amount of impurity atoms is introduced. The technique of adding these impurity atoms into semi-conductors is termed as *doping*. It is achieved either during the growth of a single crystalline semiconductor or by impurity diffusion or by ion implantation [16].

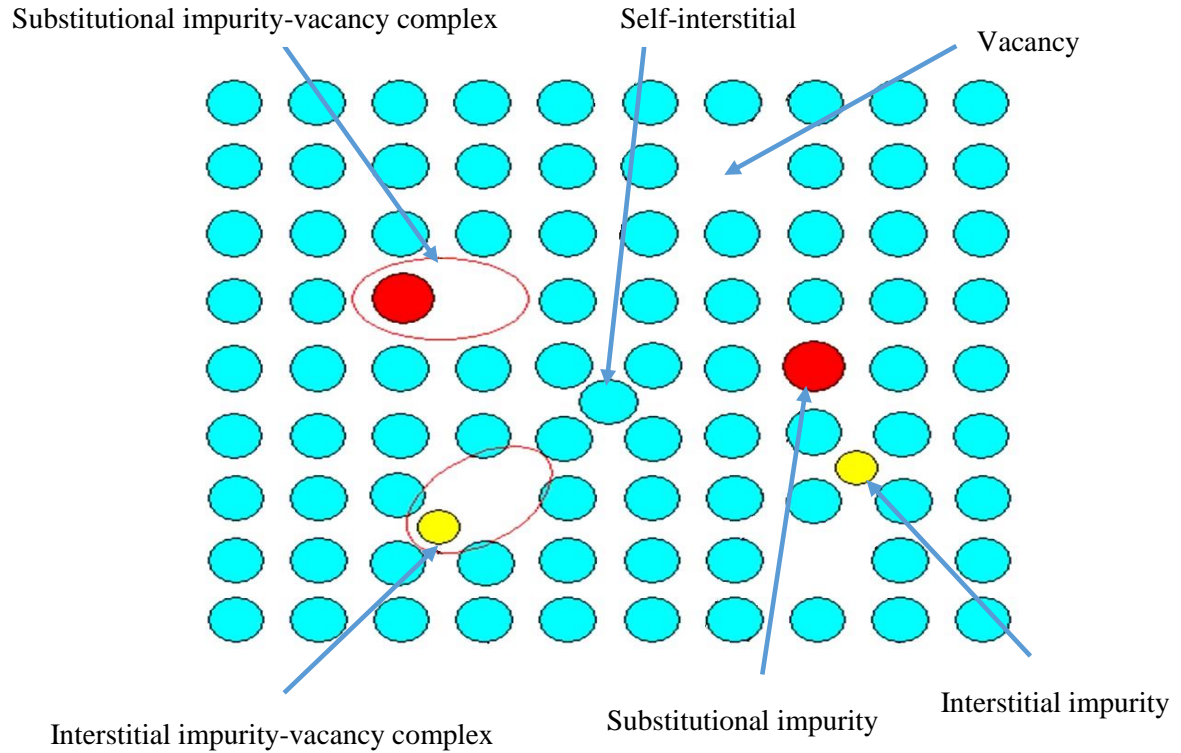


Figure 1.2: A schematic illustration of different types of point defects in a crystal lattice [16].

1.3 Literature review of Mössbauer studies in Al_2O_3

Mössbauer spectroscopy studies of Fe impurities in Al_2O_3 have been of interest over the past few decades. These studies were motivated by among other objectives, to understand the structural changes and behaviour induced by the Fe incorporation processes [17-23]. Some pioneering Mössbauer work performed on this material on low paramagnetic relaxations of Fe^{3+} impurities are well documented in refs [30-32]. Several authors [18, 27, 28] reported that at high fluences ($\sim 10^{17}$ ions/cm²), Fe was observed to be in Fe^{4+} , Fe^{3+} , Fe^{2+} , and Fe^0 states. Kobayashi *et al.* [29] performed conversion electron Mössbauer spectroscopy (CEMS) measurements at low temperature and assigned Fe^{4+} ions to fine particles of metallic iron.

The fluence dependence of the ^{57}Fe Mössbauer spectrum upon Fe-implanted on Al_2O_3 has been described by several authors. McHargue *et al.* [19], reported the fluence dependence in the range of 10^{16} - 10^{17} ions/ cm^2 , after implantation of 100-160 keV ^{57}Fe at room temperature. They observed that at low fluences the as-implanted spectrum was dominated by Fe^{2+} ions. As the fluences increased the spectrum was mainly dominated by Fe^{3+} and Fe^0 ions.

However, in the fluence dependence in the range of $(1-10) \times 10^{16}$ ions/ cm^2 after 100 keV ^{57}Fe implantation at 77 K, McHargue *et al.* [18], reported that Fe to be in Fe^{4+} , Fe^{2+} , and Fe^0 charge state and the Fe^{3+} ions were absent. Guomei *et al.* [28] performed 140 keV ^{57}Fe implantation to fluences of $(5-20) \times 10^{17}$ ions/ cm^2 and observed Fe in the Fe^{4+} , Fe^{2+} , and Fe^0 charge states for the as-implanted sample and upon annealing the Fe was found to be in Fe^{3+} , Fe^{2+} , and Fe^0 states. Recently, Dezsı *et al.* [30] confirmed by CEMS measurements of 80 keV $^{57}\text{Co}^*$ implantation to fluences of $(1-3) \times 10^{14}$ ions/ cm^2 resulted in the presence of Fe in the Fe^{3+} , Fe^{2+} , and Fe^0 charge states.

CEMS studies on the size and nature of nano-clusters formed in Fe-implanted Al_2O_3 are well documented in refs [19,31-34]. Perez *et al.* [35] reported the formation of clusters at different fluences. They observed clusters of ~2 nm sized Fe_3O_4 particles at fluences $\leq 6 \times 10^{16}$ ions/ cm^2 . An increased in fluence led to the formation of α -Fe particles sized at ~30 nm.

1.4 Aims and objectives of this study

The present project formed part of a larger study conducted by Prof. K. Bharuth-Ram (UKZN/DUT) and Prof. C. Ronning (University of Jena, Germany) on the search for magnetic cluster formation in metal oxides implanted with transition metal ions. The aim of the present study was to investigate the conditions required to achieve the formation of magnetic clusters by ion implantation of Fe into Al_2O_3 single crystal sample and focussed on Fe ions implanted with a fluence of 4 at. %, as the sample was

annealed up to 1173 K. The study sought to employ ^{57}Fe Mössbauer spectroscopy in a form of conversion electron Mössbauer spectroscopy (CEMS) as the main characterization technique, and in addition, complement the CEMS data with magnetization measurements.

1.5 Dissertation Outline

Chapter 1 gives a brief description of the properties of the material under study and of points of defects in crystals and provides a literature review of Mössbauer measurements in Al_2O_3 , which lead to the identified aims and objectives of this study. The theory of Mössbauer effect and the hyperfine interactions are discussed in **Chapter 2**. **Chapter 3** focuses on the experimental details. It describes the sample preparation and the experimental techniques employed in this study, namely CEMS and magnetization measurements using a vibrating sample magnetometer (VSM). The analysis of data obtained from CEMS and VSM measurements and the interpretation of results are presented and discussed in **Chapter 4**, which concludes with a summary of results. Finally, **Chapter 5** presents the conclusions.

CHAPTER 2

Mössbauer Effect and Hyperfine Interactions

In this chapter the basic principles of Mössbauer effect are introduced, including a discussion of the hyperfine interactions that influence observed effects, namely electric monopole, electric quadrupole and magnetic dipole interactions.

The Mössbauer effect, or recoilless nuclear resonance fluorescence, is a physical phenomenon discovered by Rudolf Mössbauer in 1958 [36]. It is a useful method for the determination of the valence state of the Mössbauer resonance atom, particularly the high-spin Fe^{2+} and Fe^{3+} states. In addition, the magnitude of the electric quadrupole splitting (for non-cubic sites) or the magnitude of the magnetic hyperfine field (for magnetically ordered crystals, or for paramagnetic systems with sufficiently long electronic relaxation times) are an indication of the valence state of the resonance atom. Furthermore, since isomer shift, quadrupole splitting, and the magnetic hyperfine field are sensitive to the local atomic environment of the Mössbauer resonance atom, lattice defects in the vicinity of the Mössbauer impurity which can arise, for example, as a result of a charge-compensating process, can be investigated.

Mössbauer effect involves the resonant and recoil-free emission and absorption of gamma (γ) radiation by atomic nuclei bound in amorphous or crystalline solid. Its applications have been found in various fields of science. Because of its ability to detect weak interactions between the nucleus and its surroundings, it is a preferred technique in chemistry and physics. Detailed information on the electric and magnetic interactions of a probe nucleus and geometric structure of its environment can be extracted from the parameters that characterize the Mössbauer spectrum resulting from the hyperfine interactions between the nuclear probe and the charge density and distribution in its immediate surroundings.

2.1 The Mössbauer Effect

In an electromagnetic transition, a free nucleus of mass m in the excited state of energy, E_e , decays to the ground state of energy, E_g , by emitting a γ -ray of energy, E_γ . However, the emitted gamma ray not only takes away the energy E_γ , it also carries away momentum p_γ ($=E_\gamma/c$) and the nucleus will recoil with energy, E_R , in the opposite direction of the γ - rays as shown in Figure 2.1. The recoil energy is given by:

$$E_R = \frac{1}{2}mv^2. \quad (2.1)$$

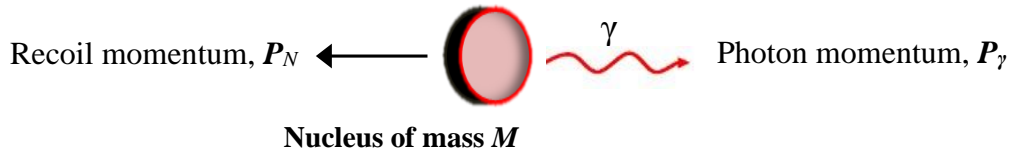


Figure 2.1: Momentum P_N and recoil energy E_R lost by a free nucleus upon γ -ray emission.

The recoil energy can be written in the form:

$$E_R = \frac{P_N^2}{2m} = \frac{E_o^2}{2mc^2}, \quad (2.2)$$

where P_N and P_γ represent the momenta of the nucleus and γ -ray, respectively, E_o is the transition energy between excited and ground states, and c is the speed of light in vacuum. The energy of the γ -ray E_γ is not equal to the transition energy E_o but is given as: $E_\gamma = E_o - E_R$. As a result, this prevents resonant emission and absorption processes between free nuclei due to insufficient γ -ray energy resulting from the loss of energy due to recoil. This is illustrated in Figure 2.2.

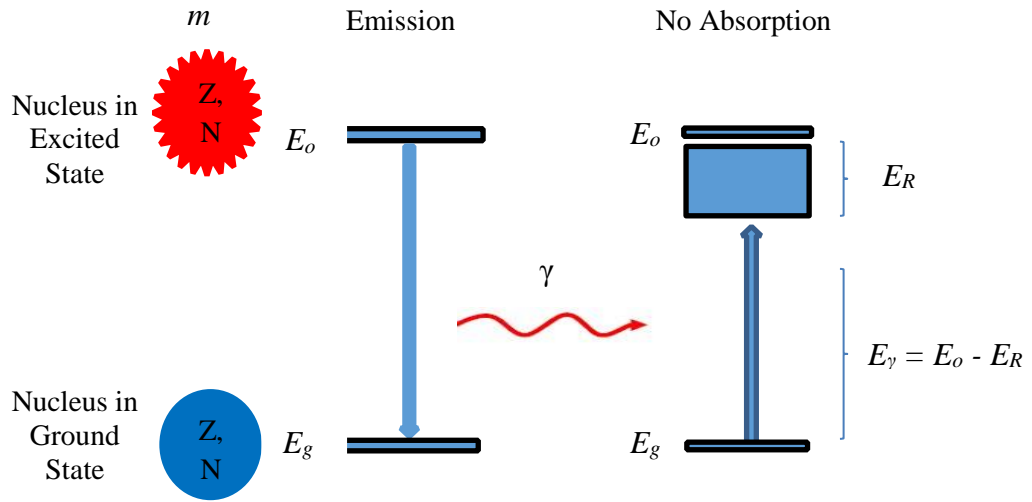


Figure 2.2: Lack of resonant γ -ray absorption due to recoil energy E_R lost to the emitting nucleus.

However, when the nucleus is rigidly bounded in a crystalline lattice of mass M , the loss in energy due to recoil becomes infinitesimally small due to the effective mass of the whole system being much greater than that of the nucleus ($M \gg m$), making E_R very small compared to E_o , resulting in nearly a recoil-free emission of the γ -ray. Figure 2.3 shows the resonant emission and absorption between two nuclei.

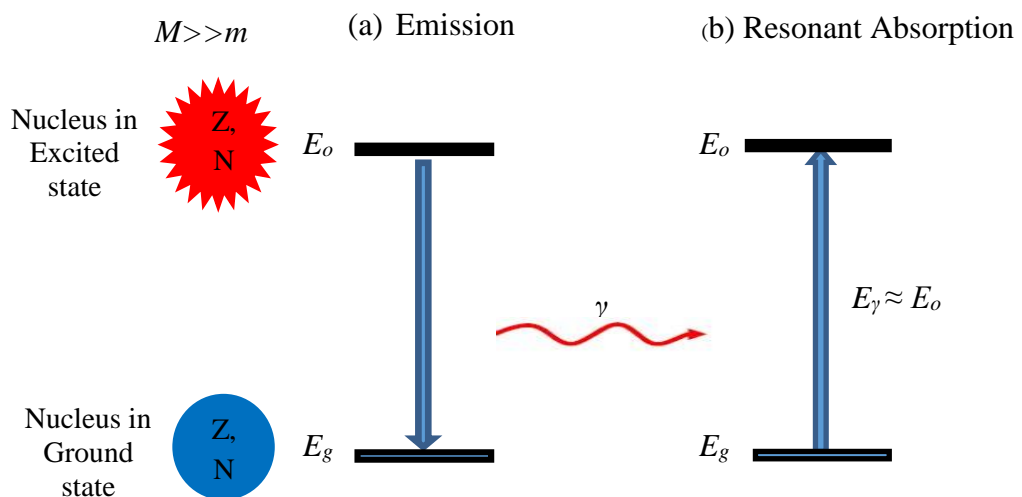


Figure 2.3: Resonant emission and absorption of a γ -ray.

2.2 Recoil free fraction

When the nucleus of gamma ray emitting (or absorbing) atom is embedded in the crystal lattice, the recoil energy is transferred to lattice vibration to the atom and then dissipated as a heat [37-39]. In an Einstein model of a solid, there exist $3N$ (N is the number of atoms) vibration modes each having frequency ω_E . Thus makes the γ -ray absorption and emission to be accompanied by the transfer of integral multiples of quantized photon energies of $0, \pm \hbar\omega_E, \pm 2\hbar\omega_E \dots$ to the lattice [37]. If $E_R \ll \hbar\omega_E$, there exist a probability of transition without lattice vibrations (zero-phonon transitions) [36]. This probability is referred to as the recoil-free fraction, f and is related to the vibrational properties of the crystal lattice by the expression,

$$f = \exp\left(-\vec{k}^2 \langle x^2 \rangle\right) \quad (2.3)$$

where $\langle x^2 \rangle$ represents the mean square vibrational amplitude of the emitting (or absorbing) nucleus in the solid along the wave vector \vec{k} . The relation between the wave vector and the momentum of the γ -ray is expressed as,

$$\vec{p}_\gamma = \frac{\hbar \vec{k}}{2\pi} \quad (2.4)$$

where h is Planck's constant. However, the momentum of the γ -ray is related to its energy and the speed of light (c) by the equation;

$$p_\gamma = \frac{E_\gamma}{c} \quad (2.5)$$

Thus, using equation (2.4) and (2.5), the wave vector can be expressed in the following form;

$$k = \frac{E_y}{\hbar c} \quad (2.6)$$

where $\hbar = h/2\pi$. Consequently, equation (2.3) can be re-written as,

$$f = \exp\left(-\frac{E_y^2}{\hbar^2 c^2} \langle x^2 \rangle\right). \quad (2.7)$$

In the Einstein model, the mean square displacement can be written as [40],

$$\langle x^2 \rangle = \frac{\langle E \rangle}{m\omega_E^2}, \quad (2.8)$$

where the mean energy $\langle E \rangle$ of the oscillators is given by the quantum number of oscillators as,

$$\langle E \rangle = \hbar\omega_E \left(\langle n \rangle + \frac{1}{2} \right). \quad (2.9)$$

$\langle n \rangle$ is the thermal average and can be expressed terms of the Bose-Einstein distribution function,

$$\langle n \rangle = \frac{1}{\exp(\hbar\omega_E/k_B T) - 1}. \quad (2.10)$$

Combining equations (2.7) – (2.10) gives the following expression for f :

$$f = \exp\left[-\frac{E_R}{k\theta_D} \coth\left(\frac{\theta_D}{2T}\right)\right]. \quad (2.11)$$

The Debye model, on the other hand, abandons the idea of the single vibrational frequency of the lattice atoms and represents a range of oscillator frequencies ranging from zero up to a maximum ω_D which follows the distribution formula $N(\omega) = \text{constant } X\omega^2$ [41].

Then the Debye model leads to the expression:

$$\bar{k}^2 \langle x^2 \rangle = \frac{\hbar}{2M} \int_0^{\omega_D} \frac{N(\omega)}{\omega} \coth\left(\frac{\hbar\omega}{2k_B T}\right) d\omega, \quad (2.12)$$

which simplifies to the following expression,

$$f = \exp\left\{-\frac{3}{2} \frac{E_R}{k_B \theta_D} \left[1 + 4 \left(\frac{T}{\theta_D}\right)^2 \int_0^{\theta_D/T} \frac{x}{e^x - 1} dx\right]\right\}, \quad (2.13)$$

where θ_D is the Debye temperature, k_B is the Boltzmann constant and T is the absolute temperature. The Debye temperature is given by:

$$\theta_D = \frac{\hbar\omega_D}{k_B}. \quad (2.14)$$

If θ_D is known, f at any temperature can be evaluated using equation (2.13). For $T \ll \theta_D$, equation (2.13) reduces to:

$$f = \exp\left[-\frac{E_R}{k_B \theta_D} \left(\frac{3}{2} + \frac{\pi^2 T^2}{\theta_D^2}\right)\right], \quad (2.15)$$

and at absolute zero ($T = 0$ K), equation (2.5) is reduced to:

$$f = \exp\left(-\frac{3E_R}{2k_B \theta_D}\right). \quad (2.16)$$

For $T > \theta_D$, f approximates to:

$$f = \exp\left(-\frac{6E_R T}{k_B \theta_D^2}\right). \quad (2.17)$$

The following can be deduced from inspecting equations (2.15) and (2.17): f is dependent on the absolute temperature and decreases with increasing temperature, f increases inversely proportionally to E_R , and f increases with an increase in the Debye temperature.

2.3. Spectral line shape and Natural linewidth

The gamma emission probability as a function of the transition energy $I(E)$, yield spectral line centered around the nuclear transition energy E_o , and have a *Lorentzian shape* as shown in Figure 2.4. If distribution of photons about E_o is given by the Breit-Wigner equation [38]:

$$I(E) = \frac{\left(\frac{\Gamma}{2}\right)^2}{(E - E_o)^2 + \left(\frac{\Gamma}{2}\right)^2}, \quad (2.18)$$

where Γ gives the Full Width at Half Maximum (FWHM) of the resonance spectral line.

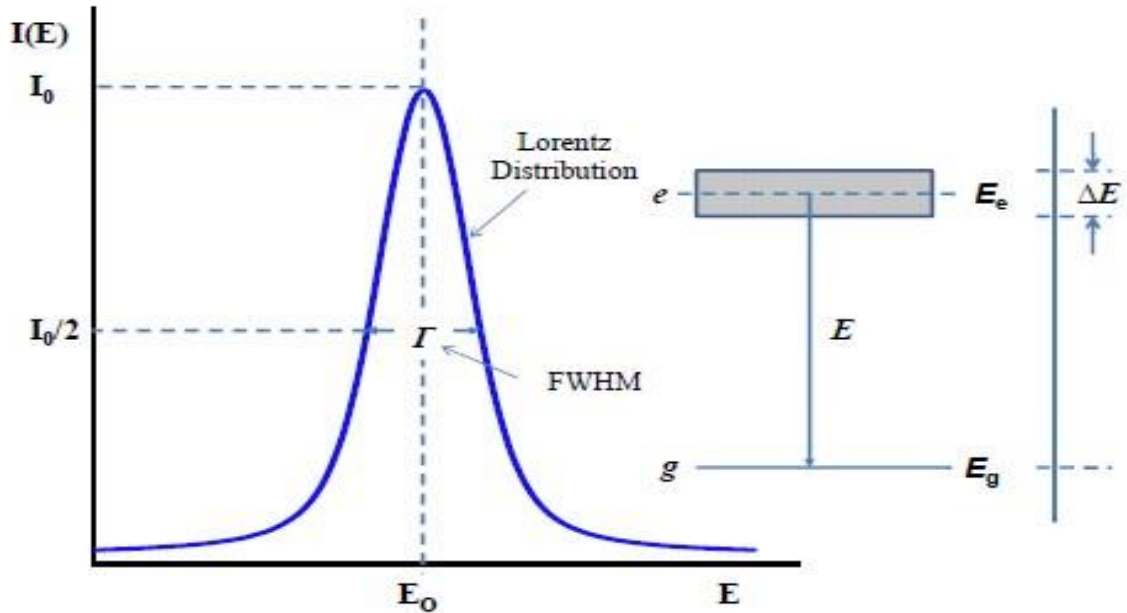


Figure 2.4: Intensity $I(E)$ plotted against transition energy E [37].

The resonance absorption cross section is given by,

$$\sigma(E) = \frac{\sigma_o \Gamma^2}{4(E - E_o)^2 + \Gamma^2}, \quad (2.19)$$

σ_o is given by the relation,

$$\sigma_o = \frac{\lambda^2}{2\pi} \frac{2I_e + 1}{2I_g + 1} \left(\frac{1}{\alpha + 1} \right), \quad (2.20)$$

where σ_o represents the maximum absorption cross section, λ is the wavelength of the γ -ray, I_g and I_e are the nucleus spin quantum numbers of respective states, and α is the internal conversion coefficient.

According to the Heisenberg uncertainty principle, the natural linewidth (Γ) is given in terms of energy uncertainty with mean lifetime τ_N :

$$\Gamma = \frac{\hbar}{\tau_N}, \quad (2.21)$$

where τ_N is related to the half-life ($t_{1/2}$) of the radioactive nucleus by the relation,

$$\tau_N = \ln 2 \cdot t_{1/2}. \quad (2.22)$$

Using equation (2.21), the linewidth for ^{57}Fe (Mössbauer nucleus) with an energy transition of 14.41 keV and mean lifetime of 141 ns will be $\sim 4.7 \times 10^{-9}$ eV. This gives an energy resolution value of approximately $\Gamma = 5 \times 10^{-9}$ eV, resulting in an energy ratio of $E_\gamma/\Gamma = 3.1 \times 10^{12}$ eV. Mössbauer spectroscopy has the highest energy resolution (5×10^{-9} eV) amongst all other spectroscopic methods [41].

2.4 Mössbauer isotope: ^{57}Fe

Since the discovery of Mössbauer effect, several elements in the periodic table have been used as Mössbauer isotopes. So far, more than 90% of Mössbauer spectroscopy publications utilizes ^{57}Fe isotope [37]. In off-line laboratory-based experiments, the Mössbauer probe is populated via the radioactive source ($^{57}\text{Co}^*$) which has a half-life of 271.74 days and decays by electron capture (EC) to the spin $I = 5/2$ excited state of ^{57}Fe . The decay scheme $^{57}\text{Co}^*$ and its daughter isotope ^{57}Fe is illustrated in Figure 2.5. $^{57}\text{Co}^*$ decays by electron capture (EC) to the 136 keV excited state of ^{57}Fe which in turn decays directly to the ground state and emits 136 keV γ -rays (15%) or decays to the 14.4 keV level and emits 122 keV γ -rays. The γ -transition for which the Mössbauer effect is observed has an energy of 14.4 keV and occurs between the first excited state $I = 3/2$ and the ground state $I = 1/2$.

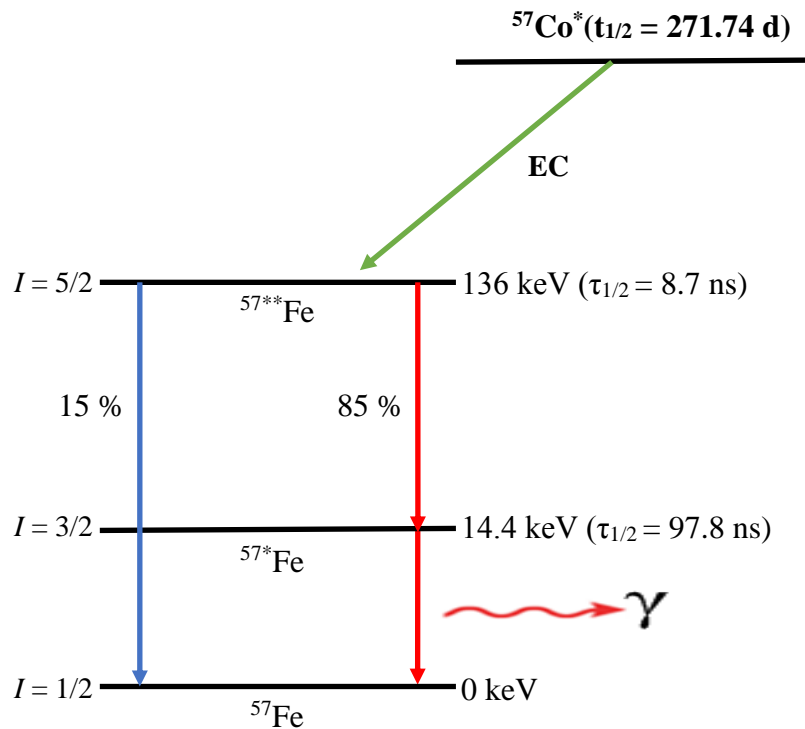


Figure 2.5: Nuclear decay scheme of ^{57}Co .

2.5 Mössbauer spectrum

A Mössbauer spectrum is measured by detecting the resonant absorption of the γ -radiation emitted in the transition to the ground state of the radioactive probe nucleus in the source by a stable nucleus of the isotope in a suitable absorber material [40]. The detection of resonant absorption is attained by increasing or decreasing the count rate at the resonant velocities in the backscattering geometry or transmission geometry. To observe the resonance between the source and the absorber, a γ -ray with variable energy is required [40]. In order to achieve this, the source is vibrated relative to a stationary absorber so that the γ -ray energy is Doppler shifted.

The level of resonant absorption at each velocity is determined by the how much of the shifted absorption energy profile overlaps with the relatively stationary energy profile spectrum [42]. Figure 2.6 shows the development of a Mössbauer spectrum. The greater the overlap, the higher the intensity of the resonant absorption line.

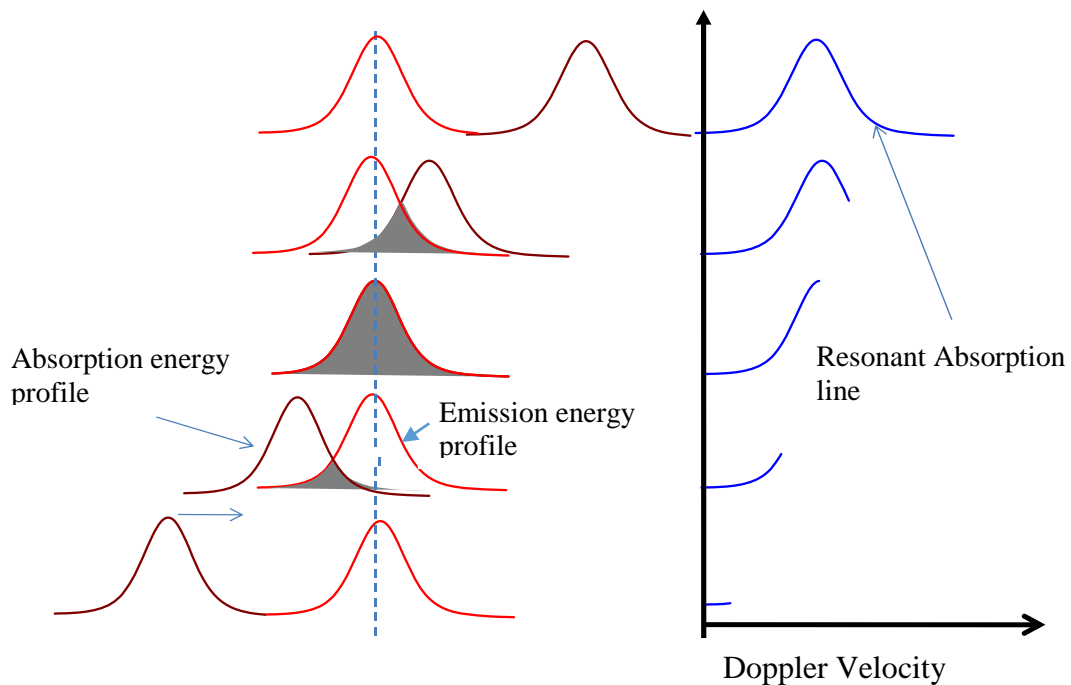


Figure 2.6: Development of a Mössbauer spectrum [42].

2.6 Hyperfine interaction parameters

Hyperfine Interactions are the interactions of the nucleus with its surrounding electrons. This interaction depends on both the density as well as the distribution of the charges in its immediate environment and can lead to finely spaced atomic energy levels called hyperfine structure. Three most important hyperfine interactions are electric monopole, electric quadrupole and magnetic dipole interactions. The electric monopole interaction will shift the energy of the levels in Mössbauer spectroscopy, and give rise to the isomer shift (δ) which is a measure of the charge difference around the probe in the source and absorber. The electric quadrupole interaction will partly split the degenerate levels and the magnetic dipole interaction will completely lift degeneracy of the levels [43].

2.6.1 Electric monopole interaction: Isomer shift (δ)

The peaks observed in a Mössbauer spectrum undergo energy shifts when the Mössbauer atom is in different materials. These shifts are due to electrostatic interaction between the nucleus and s-electrons inside the nuclear region. This interaction leads to an energy level difference between the absorber and the source nuclei. The resulting changes in the nuclear energy levels are illustrated in Figure 2.7. The transition energies E_A and E_S between the excited and the ground state in the absorber and the source are given by [37, 44].

$$E_A = \frac{3}{2} \pi Z e |\psi(0)|_A^2 [\langle r_e^2 \rangle - \langle r_g^2 \rangle] \quad (2.23)$$

and

$$E_S = \frac{3}{2} \pi Z e |\psi(0)|_S^2 [\langle r_e^2 \rangle - \langle r_g^2 \rangle], \quad (2.24)$$

where $\langle r^2 \rangle$ is the expectation value of the square of the nuclear radius, $|\psi(0)|^2$ is the probability density and Ze^2 is the nuclear charge.

Figure 2.7(b), shows the observed isomer shift in the Mössbauer spectrum as a minimum shift of the absorption line from zero velocity. When the source and absorber move relative to each other, the energy difference, ΔE between the source and the absorber, is equal to the shift caused by the Doppler effect. Then the isomer shift can be written as

$$\delta_{IS} = \frac{2\pi}{5} Ze^2 \left[|\psi_A(0)|^2 - |\psi_S(0)|^2 \right] \left[\langle r_e \rangle^2 - \langle r_g \rangle^2 \right]. \quad (2.25)$$

The most valuable information derived from the isomer shift are the oxidation state, spin state and bonding properties such as covalency and electronegativity [37]. For example, ferrous ion (Fe^{2+}) will have a greater isomer shift than ferric ion (Fe^{3+}) due to less electron density of the ferrous ion at the nuclei because of a higher shielding effect by d electrons. The isomer shift values become more positive, with a gradual increase in the number of $3d$ electrons which causes a reduction in the electron density.

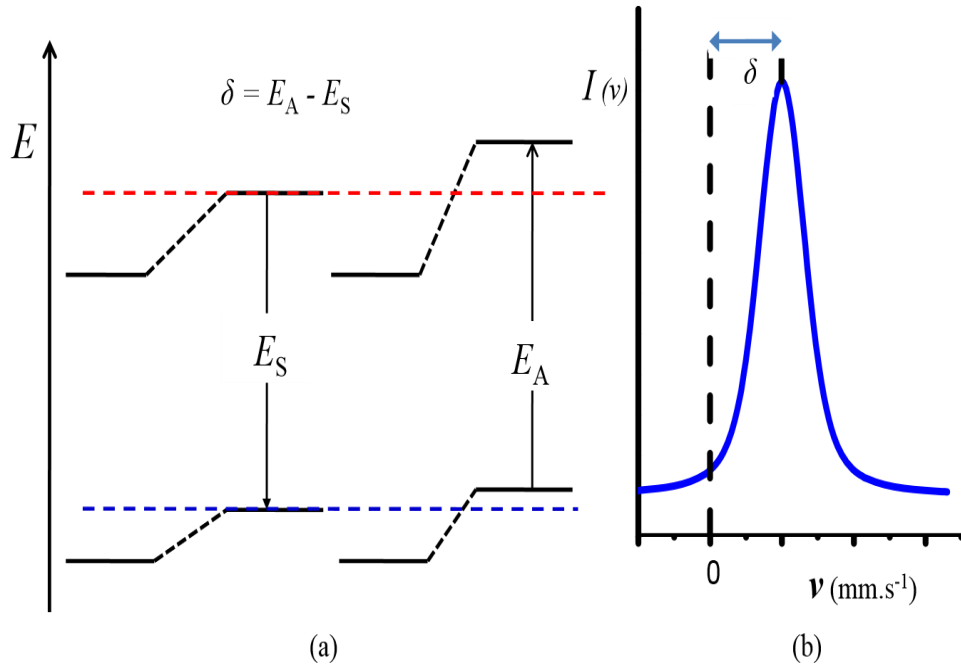


Figure 2.7: Effects of electron monopole interaction: δ represents the isomer shift [40].

Figure 2.8 shows ^{57}Fe isomer shift values as a function of oxidation states.

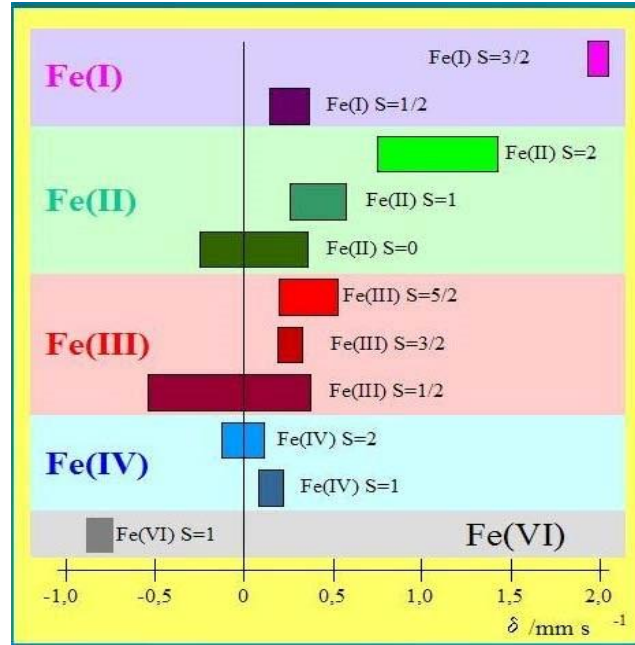


Figure 2.8: Typical isomer shift values in iron compounds [44].

The observed isomer shift is not mainly due to electric monopole interaction but also due to the thermal motion of Mössbauer atoms. These thermal vibrations give rise to temperature changes and this temperature dependent contribution causes the shift of the energy levels. This contribution is called the *second-order Doppler shift* (δ_{SOD}) and adds to the genuine isomer shift (δ) [44]. Therefore, the experimental isomer shift is given by:

$$\delta_{\text{exp}} = \delta + \delta_{\text{SOD}}. \quad (2.26)$$

The second-order Doppler shift can also be written in terms of mean square velocity $\langle v^2 \rangle$ [40, 44].

$$\delta_{SOD} = \frac{\langle v^2 \rangle}{2c^2} E_R. \quad (2.27)$$

Applying the Debye model, the shift of the energy levels due to the second-order Doppler shift can be approximated as:

$$\delta_{SOD} = \frac{-3}{2} \frac{k_B \theta_D}{mc} \left[\frac{3}{8} + 3 \left(\frac{T}{\theta_D} \right)^4 \int_0^{\theta_D/T} \frac{x^3}{e^x - 1} dx \right]. \quad (2.28)$$

2.6.2 Electric quadrupole interaction: Quadrupole splitting (ΔE_Q)

The quadrupole splitting originates from the interaction between the nuclear quadrupole moment and the electric field gradient (EFG) at the site of the nucleus. If a nucleus with $I > \frac{3}{2}$ have a non-spherical charge distribution and the nuclear quadrupole moment is defined as:

$$Q = \frac{1}{e} \int \rho(r^2) (3 \cos^2 \theta - 1) d\tau, \quad (2.29)$$

where e , is the proton charge, ρ is the charge density in the volume element $d\tau$ at a distance r from the centre of the nucleus and θ is the angle to the nuclear spin. The sign of Q can be positive and negative [43]. Positive Q means the nucleus has an elongated shape and negative Q means the shape is flattened. If the surrounding crystal has an anisotropic charge distribution there will be an electric field gradient (EFG) present at the nucleus. This will interact with the electric quadrupole moment and split the nuclear levels. The EFG is defined as a tensor:

$$V_{ij} = \frac{\partial^2 V}{\partial x_i \partial x_j}; \quad (x_i; x_j = x, y, z) \quad (2.30)$$

where V is the electrostatic potential and $(x_i; x_j = x, y, z)$ is the principal axe of the EFG.

In the absence of competing hyperfine interactions, a set of principal axes is chosen such that the off-diagonal elements of the EFG tensor are zero. By convention, $|V_{zz}| > |V_{yy}| > |V_{xx}|$ are labelled as principal axes [45], since the Laplacian of the potential vanishes,

$$V_{xx} + V_{yy} + V_{zz} = 0. \quad (2.31)$$

Then there are only two parameters to specify the EFG [46-47] and are chosen to be V_{zz} and an asymmetry parameter η of the electric field defined by,

$$\eta = \left(\frac{V_{xx} - V_{yy}}{V_{zz}} \right) \quad (2.32)$$

and must satisfy the condition, $0 \leq \eta \leq 1$. The interaction between the EFG and electric quadrupole moment is described by the Hamiltonian written in this form [44]:

$$H = \frac{eQV_{zz}}{4I(2I-1)} \left[3\hat{I}_z^2 - \hat{I}^2 + \eta(\hat{I}_x^2 - \hat{I}_y^2) \right]. \quad (2.33)$$

The isotope ^{57}Fe and ^{119}Sn have an excited-state spin $I = 3/2$ and a ground state of $I = 1/2$. For $I = 3/2$ the excited-state splits into a pair of sublevels as illustrated in Figure 2.9. The energy eigenvalues can be derived to be:

$$E_Q = \frac{eQV_{zz}}{4} \left(m^2 - \frac{5}{4} \right) \sqrt{1 + \frac{\eta^2}{3}} \quad (2.34)$$

where m is the quantum number associated with the \hat{I}_z operator.

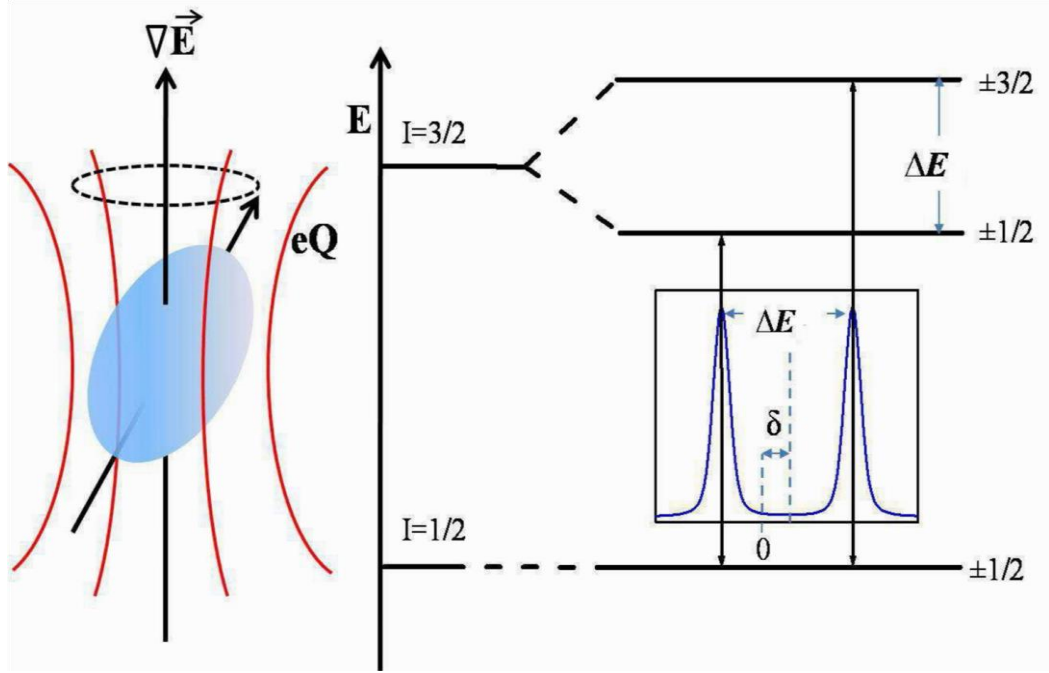


Figure 2.9: Quadrupole splitting of ^{57}Fe and the resulting Mössbauer spectrum [40].

The quadrupole splitting (ΔE_Q) between the sublevels is given by

$$\Delta E_Q = \frac{eQV_{zz}}{2} \sqrt{1 + \frac{\eta^2}{3}}. \quad (2.35)$$

As seen in equation (2.35), the quadrupole splitting is proportional to V_{zz} . For $\eta = 0$, equation (2.35) will be reduced to,

$$\Delta E_Q = \frac{eQV_{zz}}{2}. \quad (2.36)$$

Equation (2.36), shows the quadrupole splitting can either be positive or negative depending on the sign of Q and V_{zz} . For ^{57}Fe , $Q > 0$ and the sign of the quadrupole splitting solely depend on the sign of V_{zz} .

The information about the chemical bonding and whether the surrounding crystal structure is cubic ($V_{zz} = 0$) or not ($V_{zz} \neq 0$) can be obtained from quadrupole splitting [46]. The quadrupole splitting ΔE_Q is given in units of Doppler velocity (mm/s). The quadrupole interaction originates from two contributors to the total EFG is given by [45]:

$$(V_{zz})_{total} = (V_{zz})_{lat} + (V_{zz})_{val} \quad (2.37)$$

where $(V_{zz})_{lat}$ is the lattice contribution due to the charge of neighbouring ions, in a non-cubic lattice symmetry and $(V_{zz})_{val}$ is the valence electron contribution.

2.6.3. Magnetic dipole interaction: Magnetic splitting

The magnetic dipole interaction reflects the interaction between nuclear magnetic dipole moment and magnetic field \mathbf{B} at the nucleus which results in a split of the nuclear energy levels. The presence of the magnetic field at the nucleus may be due to the internal field or an externally applied field. This interaction is referred to as magnetic dipole hyperfine interaction or Zeeman splitting. The magnetic dipole hyperfine interaction can be defined by the Hamiltonian is given by the expression:

$$H_m = g_I \mu_N I \cdot \vec{B} \quad (2.38)$$

where g_I is the gyromagnetic factor of the nucleus having a nuclear spin I , μ_N is the nuclear magneton. The presence of the magnetic field leads to splitting of the states I into $2I+1$ substates characterized by the magnetic spin quantum numbers m_I [44]. The ground state with $I = 1/2$ splits into two substates ($m_I = 1/2$ and $m_I = -1/2$) and the excited states with $I = 3/2$ into four substates ($m_I = +3/2, +1/2, -1/2$ and $-3/2$) as illustrated in Figure 2.9.

The selection rules for the magnetic dipole transition ($\Delta m_I = 0, \pm 1$) allow for gamma transition between the sublevels, six possible transitions resulting in six absorption lines in the Mössbauer spectrum. The energies of the sublevels are given by first-order perturbation theory:

$$E_m(m_I) = -g\mu_N \vec{B} m_I. \quad (2.39)$$

The magnetic hyperfine splitting allows for the determination of the magnitude and direction of the effective magnetic field \vec{B}_{eff} acting at the nucleus. The effective magnetic field is given as a sum of two contributors [42]:

$$\vec{B}_{eff} = \vec{B}_{loc} + \vec{B}_{hf} \quad (2.40)$$

where \vec{B}_{loc} is the local magnetic field at the Mössbauer nucleus and \vec{B}_{hf} is the hyperfine magnetic field of the Mössbauer atom's own electrons. Furthermore, B_{loc} can be expressed in terms of the following contributions [38].

$$\vec{B}_{loc} = \vec{B}_{ext} - \vec{D}_m + \frac{4\pi}{3} \vec{M}_m, \quad (2.41)$$

where B_{ext} is an external field, \vec{M}_m is the magnetization, D_m is the demagnetization field and the term $4\pi/3 \vec{M}_m$ is the Lorentz field. The magnetic hyperfine field B_{hf} has three contributions [37-38]:

$$\vec{B}_{hf} = \vec{B}_F + \vec{B}_L + \vec{B}_D, \quad (2.42)$$

where \vec{B}_F is Fermi contact field from s-electron spin density, \vec{B}_L is the orbital field due to the orbital motion of unpaired electrons and the nucleus and \vec{B}_D is the dipole field at the nucleus stemming from the total spin magnetic moment of the valence electrons.

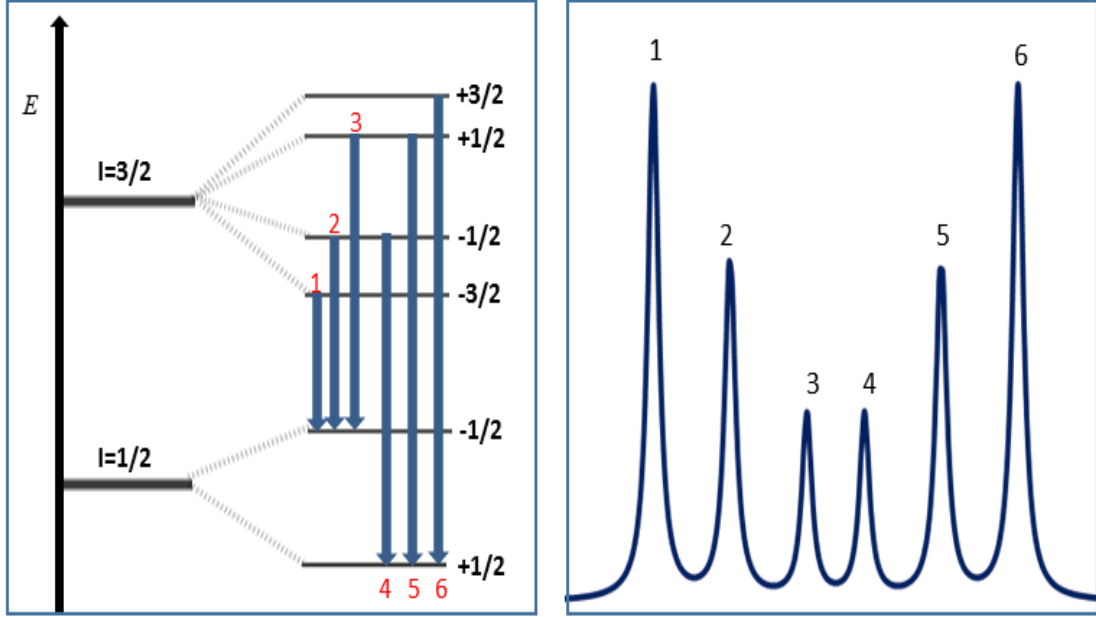


Figure 2.10: Magnetic splitting of $I = 1/2$ and $I = 3/2$ the corresponding sextet observed in a typical spectrum [47].

2.6.4 Combined magnetic and quadrupole interactions

If both the magnetic and quadrupole interactions are present, then the combined effect will yield a complex spectrum as illustrated in Figure 2.11. For a $\frac{1}{2} \rightarrow \frac{3}{2}$ decay, the quadrupole interaction can be treated as a first order perturbation to the magnetic interaction provided the EFG tensor is axially symmetric. The eigenvalues of the energy levels are given by [48].

$$E_{Q,m} = -g\mu_N B m_I + (-1)^{|m_I|+1/2} \frac{eQV_{zz}}{8} (3\cos^2 \theta - 1) \quad (2.43)$$

where θ is the angle between the magnetic axis and EFG tensor axis and the last term is called the quadrupole shift ϵ . The electric quadrupole interaction strength eQV_{zz} is not determinable from the spectrum in this case, unless the direction of magnetization relative to the symmetry axes is measured by other means [48].

If the electric quadrupole is known, the experimental results obtained can be used to determine the direction of the magnetization. In cases such as ferric and metallic systems [48], electric quadrupole interaction does not depend on temperature or it varies slowly with it, and the value determined above the magnetic order can be used to determine the orientation of the magnetization vector with respect to the EFG tensor. If EFG tensor is not axially symmetric but the magnetic axis lies along one of its principal axes, then the excited state splitting for $I = 3/2$ are given by four energy:

$$E = \pm \frac{1}{2} g \mu_N B \pm \frac{e Q V_{ZZ}}{4} \left[\left(1 + \frac{4 g \mu_N B}{e Q V_{ZZ}} \right)^2 + \frac{\eta^2}{3} \right]^{\frac{1}{2}} \quad (2.44)$$

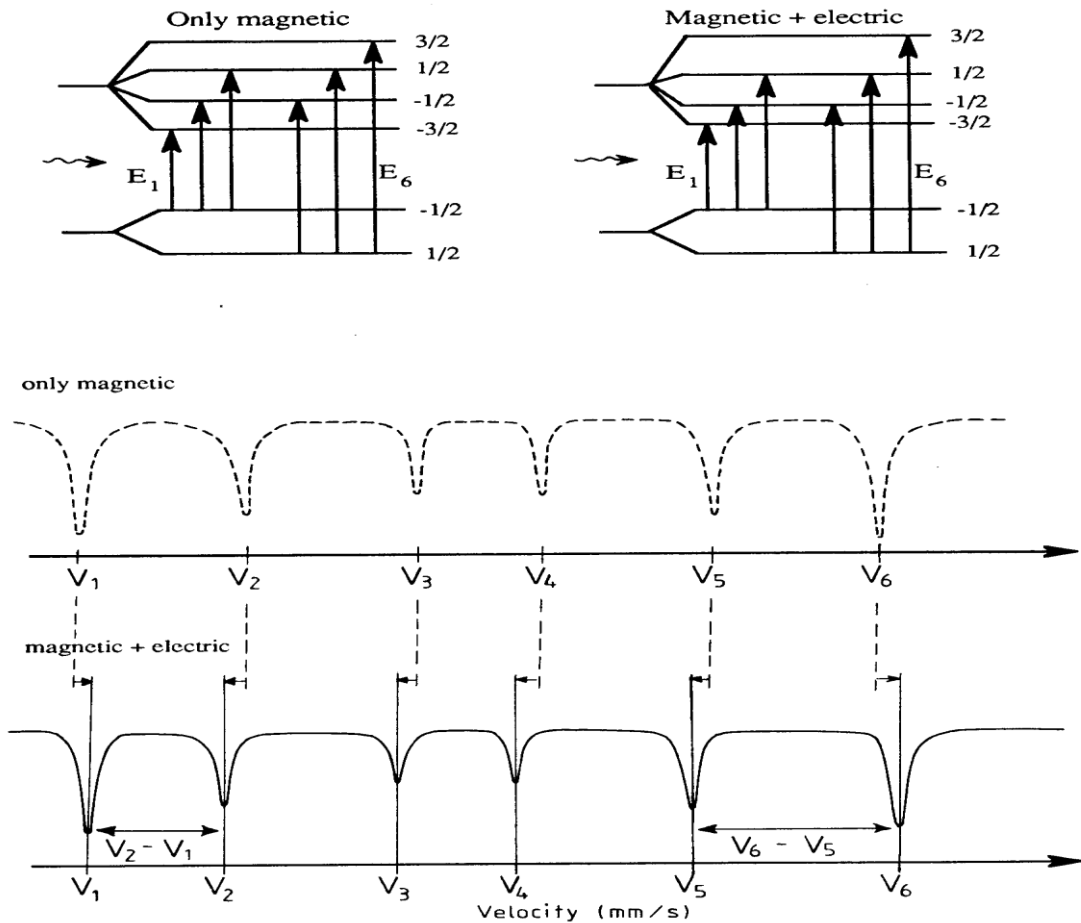


Figure 2.11: δ and ΔE_Q when only the magnetic dipole interaction is present and when the magnetic dipole interactions is perturbed by a small electric quadrupole interaction [48].

A combined magnetic and quadrupole interaction can more information regarding the symmetry of the atomic environment and the relative orientation of the magnetization with respect to the axes.

2.6.5 Angular dependence of hyperfine parameters

2.6.5.1 Quadrupole splitting

The complexity of the Mössbauer spectrum can be simplified if the relative line intensities of various spectral components are known. These components (either doublet or sextet) can show an angular dependence of the relative line intensities of the split lines. For a quadrupole split doublet in a polycrystalline material, the two observed lines will have equal intensities in the Mössbauer spectrum [46]. However, a quadrupole split doublet measured in single-crystalline material may exhibit an angular dependence of the relative line intensities. The two transitions labelled π and σ depends on the angle between the principal axis of the EFG and the γ -direction. Therefore, the ratio of the intensities between $\pi : \pm 1/2 \rightarrow \pm 3/2$ and $\sigma : \pm 1/2 \rightarrow \pm 1/2$ transitions is given by,

$$f(\theta) = \frac{I_\pi}{I_\sigma} = \frac{3(1 + \cos^2 \theta)}{5 - 3\cos^2 \theta}, \quad (2.44)$$

where θ is the angle between the γ -ray direction and the V_{zz} direction. For $\theta = 90^\circ$ and $\theta = 0^\circ$, $f(\theta)$ will be 0.6 and 3.0 respectively. However, if $\theta = 54.7^\circ$ (magic angle), $f(\theta) = 1$ which means the intensity of the two peaks is equal. The sign of the ΔE_Q depends on the sign of the V_{zz} of the EFG, which can either be positive or negative depending on whether $m_I = \pm 3/2$ energy level is higher or lower than the $m_I = \pm 1/2$ energy level. The intensity of the leg of the asymmetric doublet can be determined by the sign of the EFG and geometry of the experimental set-up. If $\Delta E_Q > 0$, the left leg is more intense at small angles in emission geometry, while the right leg is more intense at

small angles in transmission geometry [40]. If $\Delta E_Q < 0$, the reverse is also true. Table 2.1 shows the transition probabilities for the quadrupole splitting doublet in a Mössbauer spectrum.

Table 2.1: Transition probabilities for the quadrupole split doublet in a Mössbauer spectrum [46].

Transition	Line position for $\Delta E_Q > 0$	Relative intensity	Poly-crystalline
$\pi : \pm 1/2 \rightarrow \pm 3/2$	$-\delta - \Delta E_Q/2$ (left peak)	$3 + 3\cos^2 \theta$	4
$\sigma : \pm 1/2 \rightarrow \pm 1/2$	$\delta + \Delta E_Q/2$ (right peak)	$5 - 3\cos^2 \theta$	4

2.6.5.2 Magnetic splitting

In magnetic sextets originating from single crystal materials, the relative intensity ratio depends on the angle θ between the magnetic hyperfine field and emission γ -direction. Table 2.2, shows the relative intensity ratios of the sextet lines for the ^{57}Fe transition ($I = 3/2 \rightarrow 1/2$).

Table 2.2: Angular distribution of the relative intensities for the six allowed transitions in ^{57}Fe [40].

Line	Transition	Relative intensity	Poly-crystalline	$\mathbf{B} // \gamma$	$\mathbf{B} \perp \gamma$
1 (6)	$\pm 1/2 \rightarrow \pm 3/2$	3	3	3	3
2 (5)	$\pm 1/2 \rightarrow \pm 1/2$	$4\sin^2 \theta / (1 + \cos^2 \theta)$	2	0	4
3 (4)	$\pm 1/2 \rightarrow \pm 1/2$	1	1	1	1

From Table 2.2, it is seen that only the intensity of line 2 and 5 vary from 0 to 4 and are angle dependent. When $\theta = 0^\circ$, the ratio of relative intensities of the sextet lines is 3:0:1:1:0:3, and when $\theta = 90^\circ$ the ratio is 3:4:1:1:4:3. For α -Fe foil the magnetic field is randomly orientated, resulting in a sextet of line ratio close to 3:2:1:1:2:3.

CHAPTER 3

Experimental Details

3.1 Introduction

This chapter briefly describes the preparation of the sample by ion implantation which is employed to incorporate dopant atoms in the substrate under study. The ion implantation process has several advantages: (i) controlled dopant concentration, their lateral and depth distribution, (ii) controlled substrate temperature which limits diffusion of the implanted species, (iii) complex profiles can be achieved by multi-energy implants, and (iv) less sensitive to surface cleaning procedures. A detailed theory of ion implantation and its application in semiconductors is outlined in refs [49-52].

Two characterization techniques were utilized in this study, namely, Mössbauer spectroscopy (MS) and magnetization measurements with a vibrating sample magnetometer (VSM). Since its discovery (in 1957), Mössbauer spectroscopy has found wide applications both in industrial and research studies [44, 53-55]. Mössbauer spectroscopy specific experimental details of the measurements undertaken are discussed as being the main technique employed as Conversion electron Mössbauer (CEMS) on $^{57}\text{Fe}/^{56}\text{Fe}$ implanted sample using a standard 50 mCi $^{57}\text{Co}(\text{Rh})$ source. In addition, VSM as a secondary technique was employed to investigate the magnetic properties of the sample under study. A summary of the principles of Mössbauer spectroscopy is presented together with a brief introduction of the principle of operation of a vibrating sample magnetometer.

3.2 Sample Preparation

The ion implantation technique is a general method for altering the near-surface properties of a wide range of materials [50]. During implantation, impurity atoms are

accelerated from few a keV to several hundreds of keV energies and implanted into crystalline sample [56].

As these high-energy atoms enter the crystal lattice, they lose energy due to collisions with the lattice atoms before coming rest some distance below the surface of the substrate. Ion implantation has proved to be a success thus far in the area of semiconductor technology, and today almost all semiconductors devices are fabricated using one or more ion implantation steps [50]. Although various articles [57-59] have been published on research and development involving ion implantation, this technique has also proven to be successful as a means of modifying the physical and chemical properties of the near-surface region of metals and alloys [60-61].

The focus of the present project was to search for the formation of magnetic nanoclusters of Fe ions implanted in Al_2O_3 . The incorporation of the Fe ions in the crystal was achieved by implanting a combination of ^{57}Fe and ^{56}Fe ions to total atomic concentration of 4 at. % of Fe in the Al_2O_3 single crystal substrate. ^{57}Fe is a Mössbauer probe nucleus, and hence its presence assured that the implanted sample could be studied by using Mössbauer spectroscopy. The implantations of the Fe ions accelerated to 50 keV energy, were carried out at the University of Jena, Germany, using the ROMEO implanter. The implantations were performed at room temperature in an implantation chamber under vacuum with a pressure $<3.0 \times 10^{-6}$ mbar with the sample tilted at an angle of 7° to the surface normal of the substrate to avoid channeling effects.

3.2.1 Implantation Parameters, and Profiles

Monte Carlo simulations were carried out to predict the implantation profile using the code SRIM2013 [62]. The implantation parameters were chosen carefully following SRIM2013 simulations to achieve an implantation profile (see Figure 3.1) and a combined 4 at. % concentration of Fe ions, aimed at keeping lattice damage relatively low and allowing enough transition metal ions in the Al_2O_3 lattice to give measurable magnetization signals.

The implantation energies and fluences are listed in Table 3.1 below while Figure 3.2 (a) and Figure 3.2 (b) show the distribution profiles of ^{57}Fe and ^{56}Fe implanted into Al_2O_3 . The target displacements, vacancies, and replacement collisions produced as the result of the simulations are presented in Figure 3.3 (a) and Figure 3.3 (b).

Table 3.1: Energy and fluences of iron species implanted in Al_2O_3 .

Ion	Energy (keV)	Fluences ($\times 10^{15} / \text{cm}^2$)
^{56}Fe	50	5.6
^{57}Fe	50	5.6

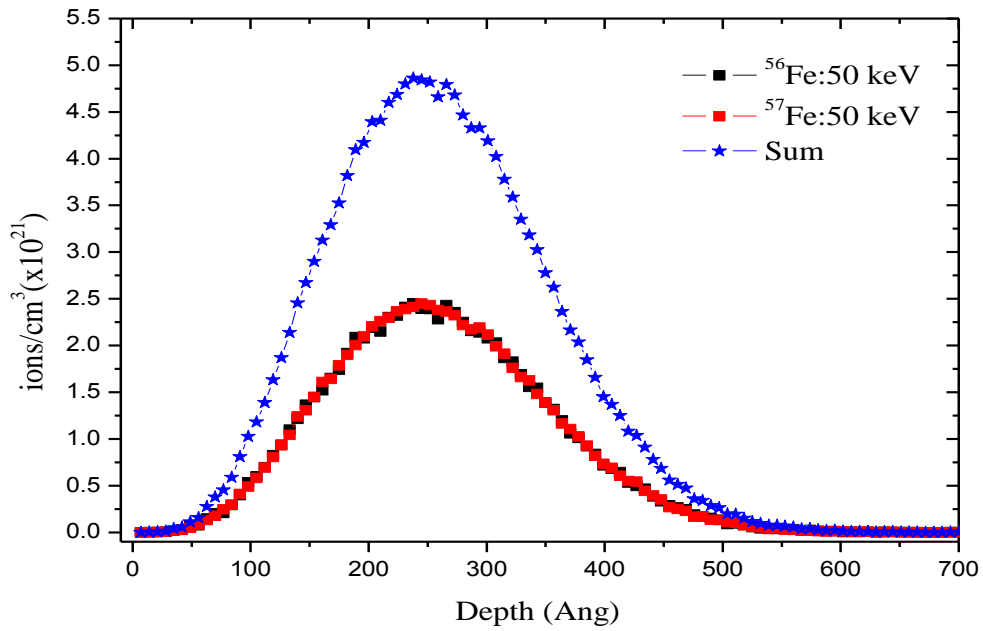


Figure 3.1: Plot of concentration distribution of implanted Fe in Al_2O_3 , estimated from TRIM simulations.

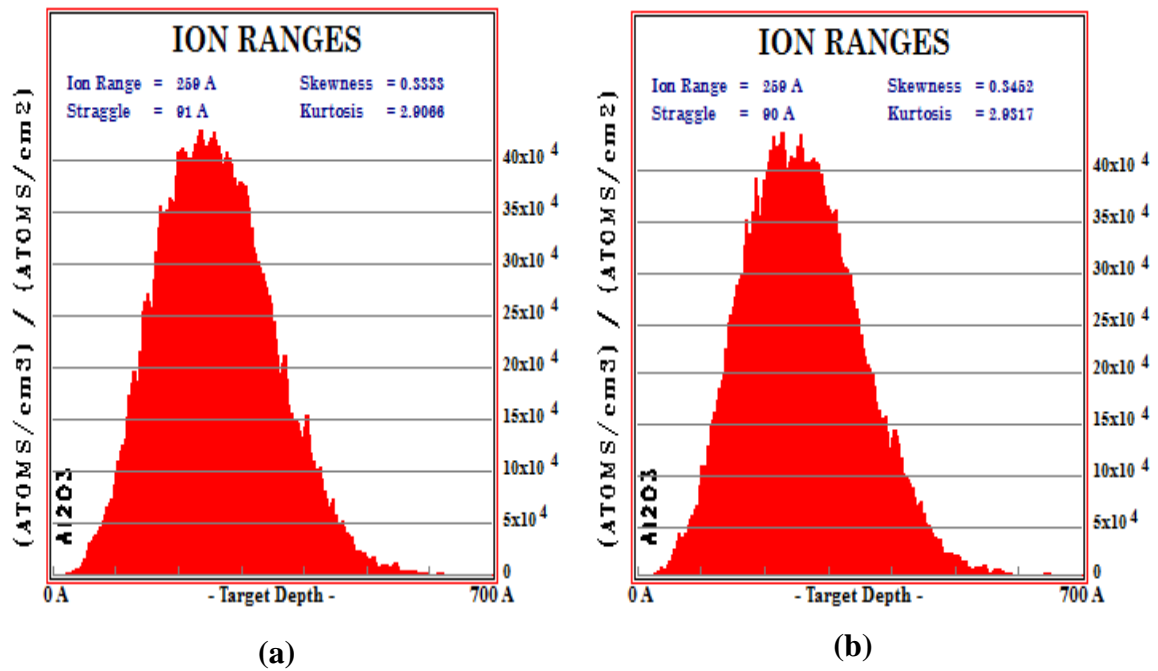


Figure 3.2: Ion distribution profiles for 50 keV of (a) ^{56}Fe and (b) ^{57}Fe implanted at an angle of 70° in Al_2O_3 .

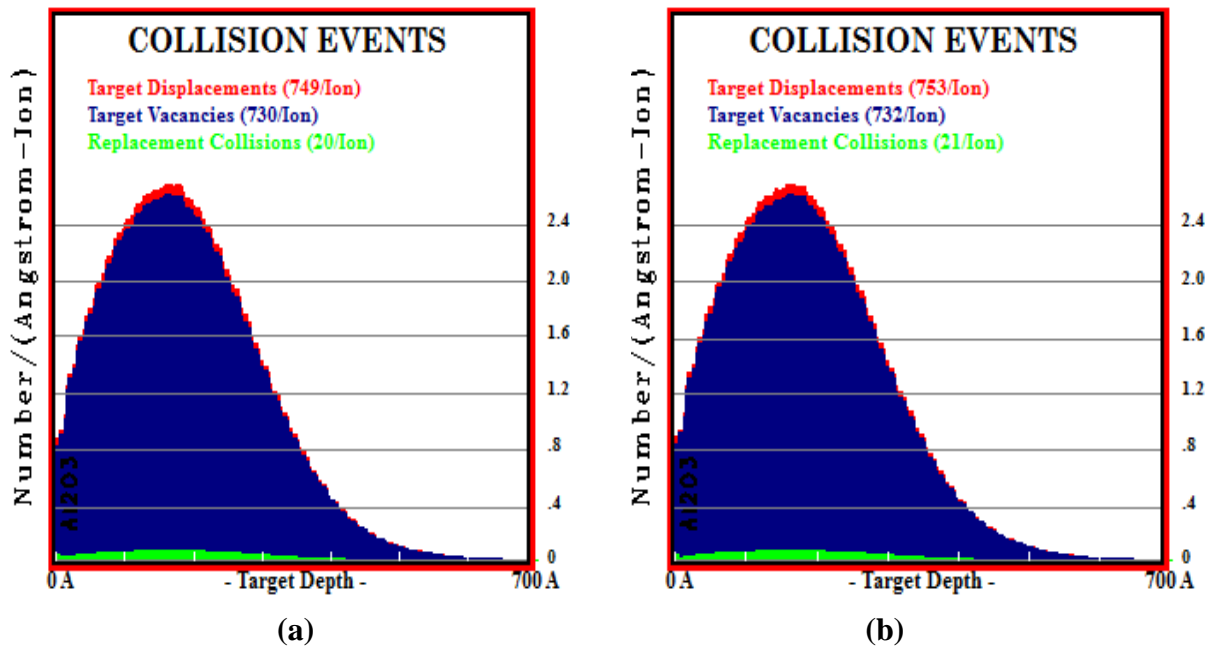


Figure 3.3: Damage profiles for 50 keV of (a) ^{56}Fe and (b) ^{57}Fe implanted at an angle of 70° in Al_2O_3 .

The calculated projected range and straggle values for Al₂O₃ implanted with ⁵⁶Fe and ⁵⁷Fe are displayed in Table 3.2 below.

Table 3.2: Projected range and straggle for Al₂O₃ implanted with ⁵⁶Fe and ⁵⁷Fe.

	Al ₂ O ₃ implanted with ⁵⁶ Fe		Al ₂ O ₃ implanted with ⁵⁷ Fe	
Projection	Range (Å)	Straggle (Å)	Range (Å)	Straggle (Å)
Longitudinal	259	91	259	90
Lateral	61	77	60	77
Radial	90	52	90	51

3.3 Mössbauer spectroscopy

⁵⁷Fe Mössbauer spectroscopy was utilized as the main characterization technique in this study. Due to its unique feature, Mössbauer spectroscopy has the ability to probe location environment at atomic scale, and provide reliable information on the lattice sites, symmetry, charge state, and magnetic interactions of the Mössbauer isotope [42]. In this study, conversion electron Mössbauer spectroscopy (CEMS) was employed and is discussed in detail in the following section.

3.3.1 Conversion Electron Mössbauer Spectroscopy (CEMS)

CEMS is a technique which can be used to investigate Mössbauer effect in back-scattering geometry by detecting the conversion electrons emitted in the decay of the Mössbauer probe nucleus. Figure 3.4, illustrates the internal conversion process in the decay of the excited state of iron nucleus. During the process, the γ -ray photon transfers its energy to electrons from the K, L or M electronic shells. Holes in the L shell to K shell are filled by transition of electrons by higher levels, resulting in emission of X-

rays and Auger electrons. CEMS detector is mostly sensitive to low energy electrons. In the case of internal conversion electron detection, CEMS detector will detect the emitted K-electrons because of close proximity of these electrons to the nucleus. An iron K-conversion electron is ejected with a kinetic energy equivalent to the difference between the gamma ray energy and binding energy [16].

CEMS techniques are normally restricted to the near-surface of the sample than bulk, due to the low kinetic energy of the K-electrons. It is also useful for samples with thick substrates or high Z where transmission of γ -rays through a sample is blocked. Thus, it is useful in studying implanted samples [16, 63]. The advantage of CEMS compared with Transmission Mössbauer Spectroscopy (TMS) is that samples of any shape and thickness can be used.

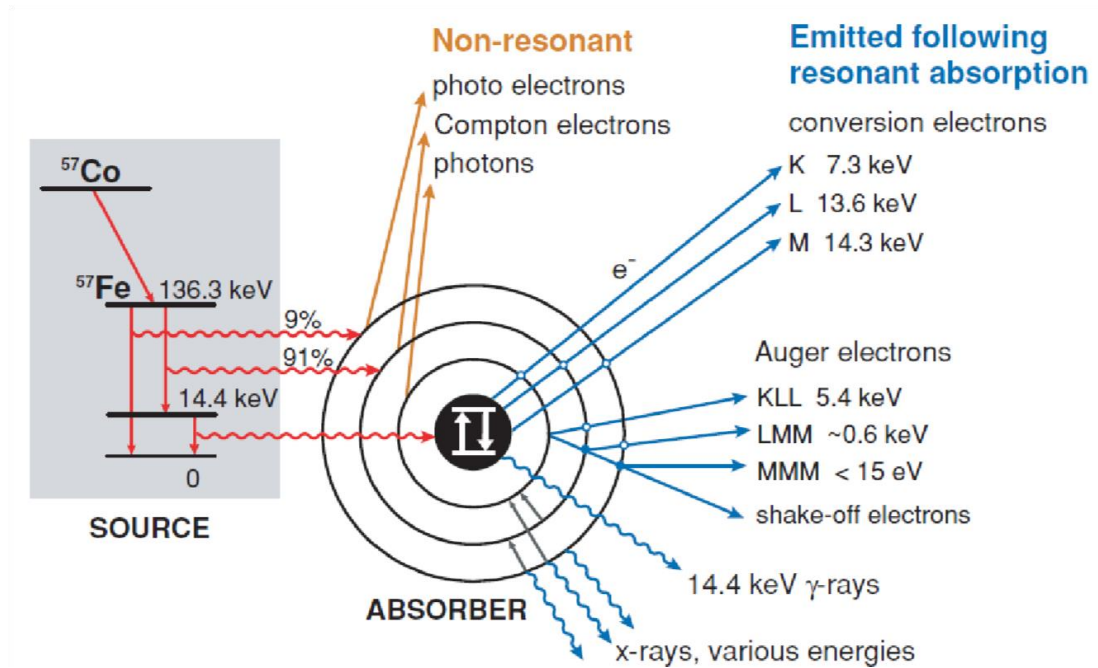


Figure 3.4: The nuclear decay scheme for $^{57}\text{Co}/^{57}\text{Fe}$ and various emission processes for ^{57}Fe that can follow resonance absorption of an incident gamma photon [64].

Figure 3.5, shows the CEMS system at the Mössbauer laboratory at iThemba LABS. The parallel plate avalanche detector (PPAD) being mounted on the gas tank. A number of lead blocks were placed around the experimental set-up for radiation protection to about 90% of γ -rays emitted from the source and the sample.

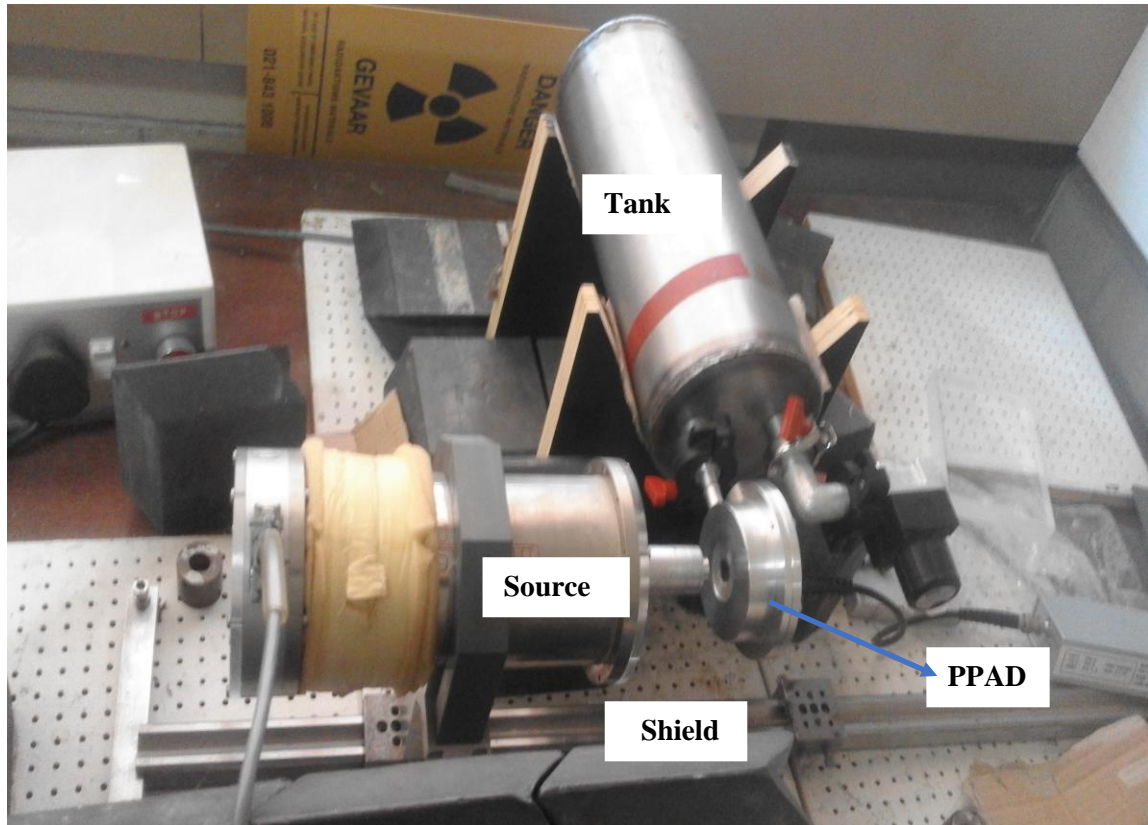


Figure 3.5: CEMS set-up at iThemba LABS.

3.3.2 CEMS Measurements and Annealing Conditions

CEMS measurements were carried out at room temperature using a ^{57}Co (Rh) source on the as-implanted sample and after annealing at temperatures up to 1173 K. The sample was annealed for 30 minutes in air at atmospheric pressure.

3.3.3 CEMS Detector

Many different types of CEMS detectors were developed and used in Mössbauer spectroscopy. The most common CEMS detectors are (a) single/multiple wire anode gas low detectors and (b) parallel plate avalanche detectors (PPAD).

In this present work, a PPAD developed by Moodley and Bharuth-Ram [64] was used as a CEMS detector. As shown in Figure 3.6 below, γ -rays from the source strike a sample incorporated in the PPAD. The sample to be probed is placed in the PPAD on one of the plates which is negatively charged as shown in Figure 3.6.

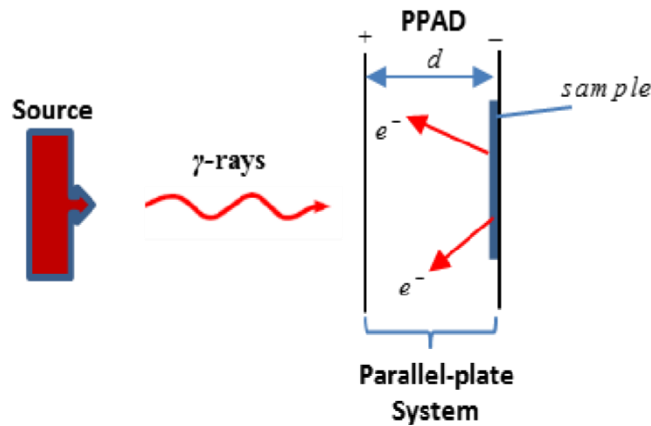


Figure 3.6: Schematic diagram of a PPAD with a source of γ -ray.

Figure 3.7 below, shows how the sample under investigated was mounted on of the negatively charged plate in the PPAD. The plates were made of Perspex and were sprayed with graphite to make them conducting.

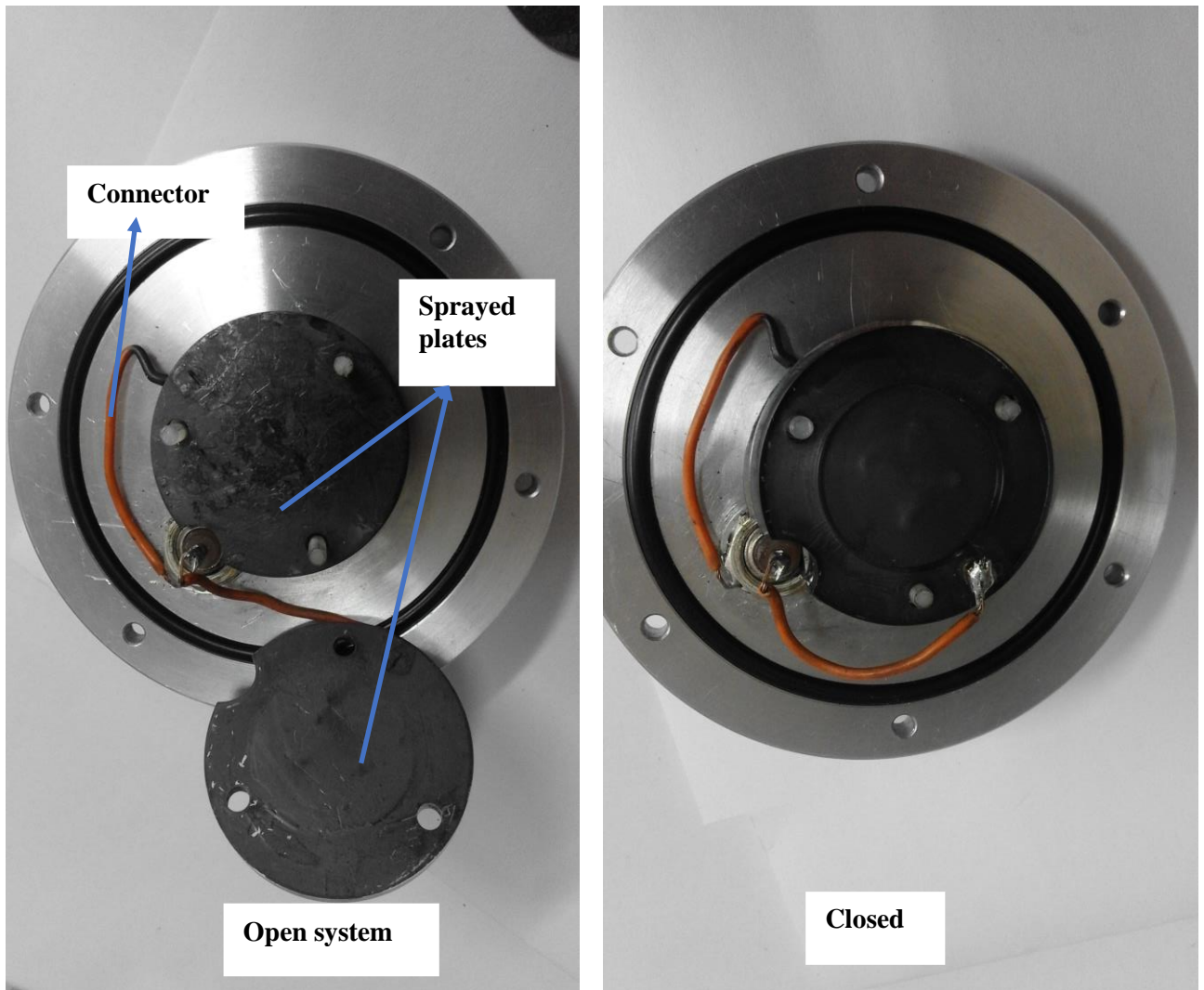


Figure 3.7: PPAD open and closed systems.

3.3.4 Procedure of operation in CEMS

- 1). The sample under investigation was placed on the graphite conducting region of one perplex plate then mounted as shown in Figure 3.8.



Figure 3.8: Sample mounted on PPAD.

-
- 2). The detector was then connected to the cylindrical container filled with pressure as shown in Figure 3.9.

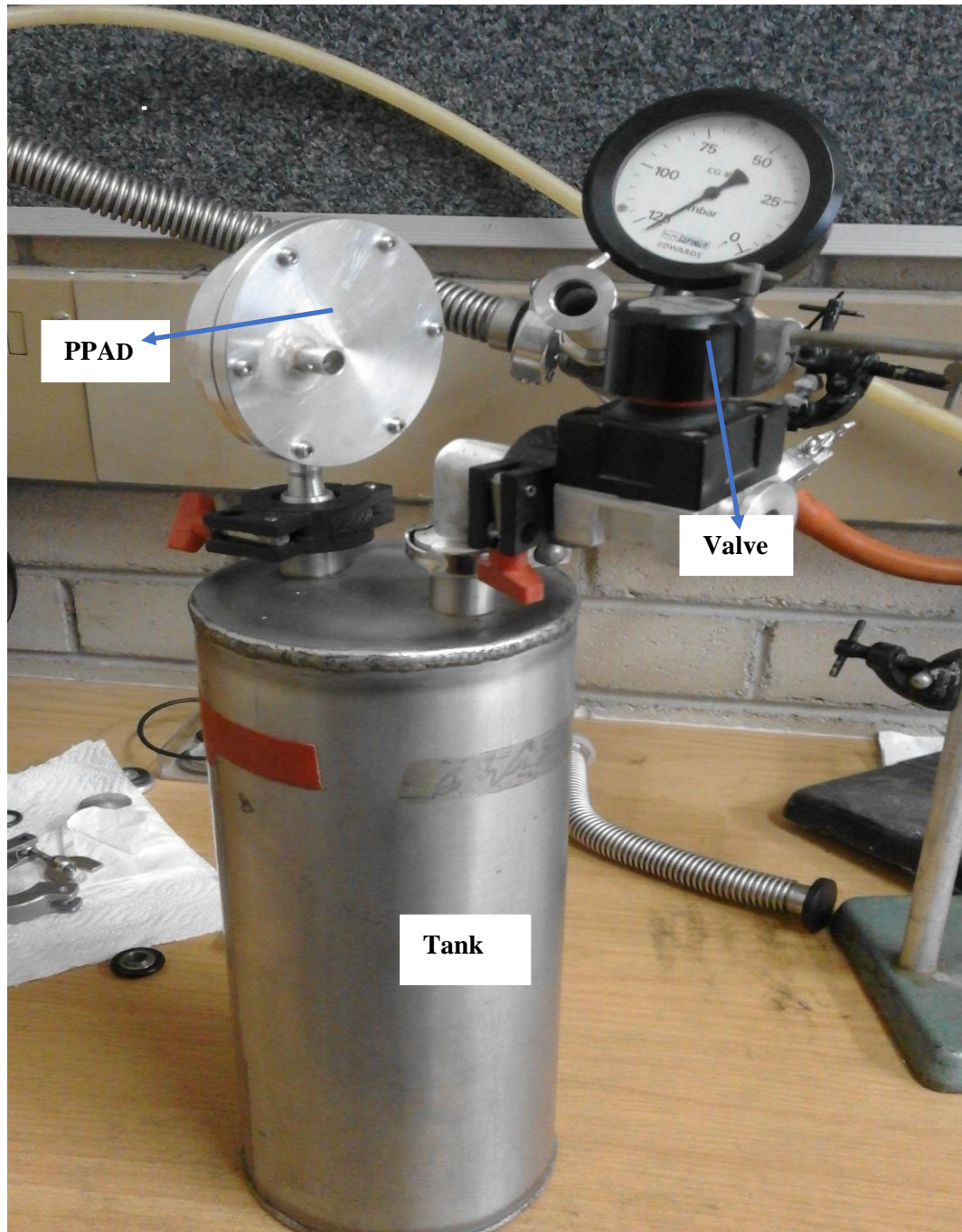


Figure 3.9: PPAD connected to a tank.

-
- 3). Figure 3.10, shows connections between, the tank, PPAD, the vacuum pump and the connections to the flask containing the acetone.

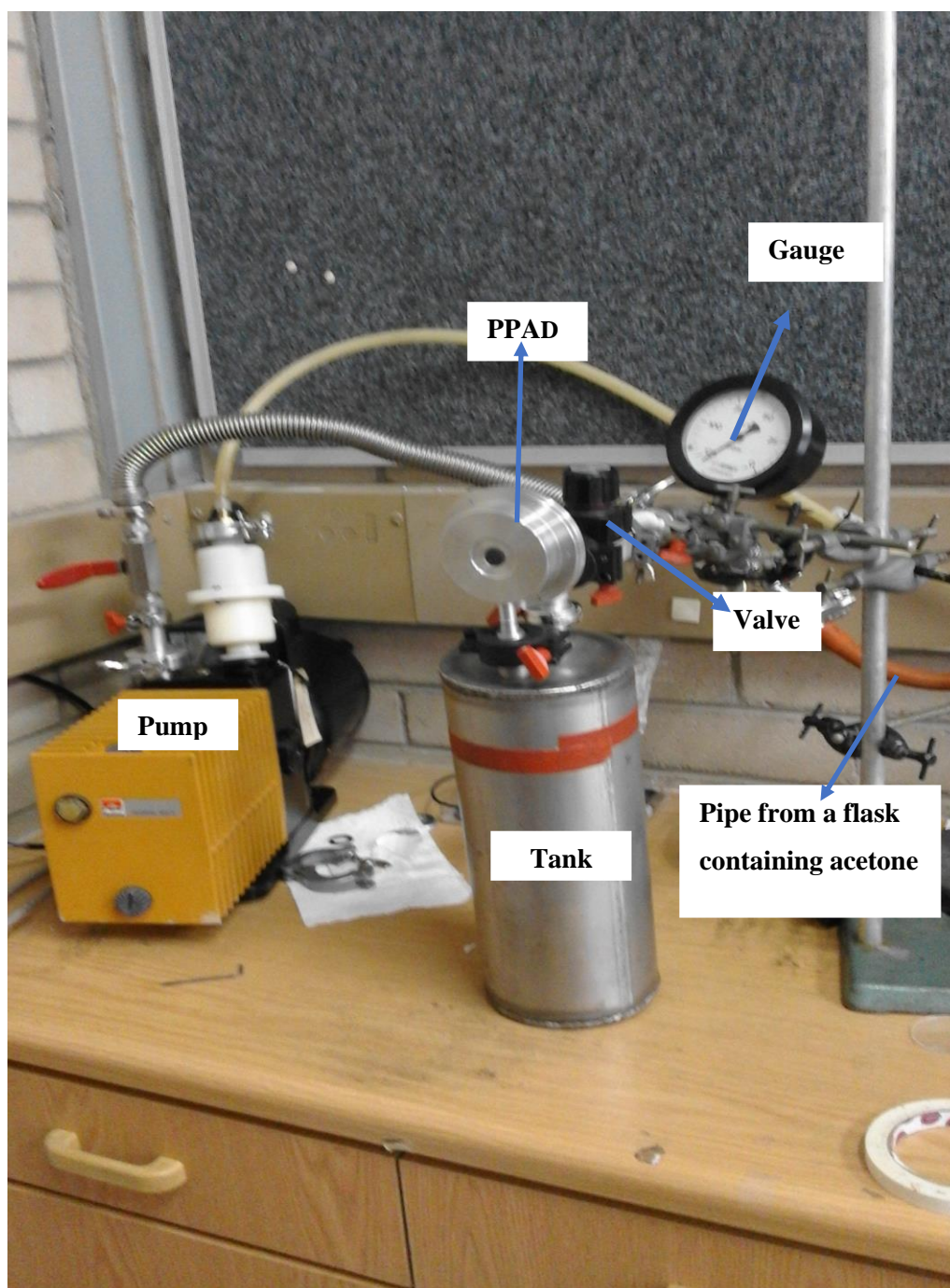


Figure 3.10: Vacuum pump station at iThemba LABS Mössbauer laboratory.

-
- 4). After a sequence of pumping and flushing of the detector volume with acetone vapour, the pressure was set at the desired value of 35 mbar.

3.3.5 Data acquisition Electronics

The experimental set-up and instrumentation of the CEMS system are illustrated in Figure 3.11.

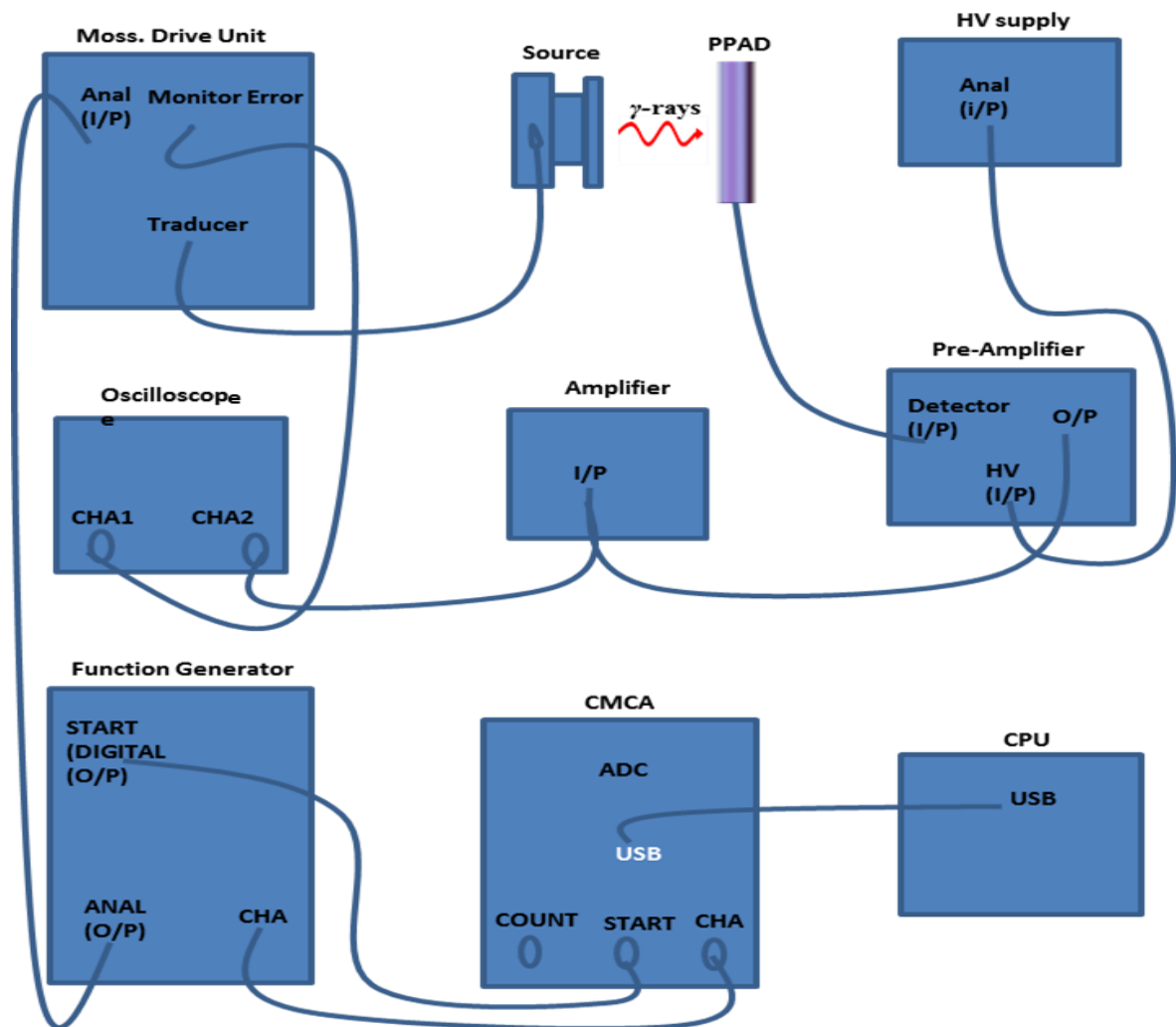


Figure 3.11: Electronics and Experimental set-up for CEMS [47].

The parallel-plates in the detector are connected to a high voltage (HV) supply through the pre-amplifier. The pulses from the detector is pre-amplified, then amplified and passed through the single channel analyzer (SCA). The SCA rejects the background radiation and retains only a pulses corresponding to 14.41 keV Mössbauer γ -gamma rays [65]. The discriminated pulses are finally fed into a multi-channel analyzer (MCA), which operates in pulse height analysis (PHA) mode and multichannel scaling (MCS) mode. The PHA mode is used to observe the total energy spectrum of the radiation source and allow the selection of 14.41 keV line.

The MCS mode synchronizes several hundreds of channels with the velocity of the Mössbauer drive unit (MDU) by making use of the feedback control system through the function generator (FG). The FG produces the reference signal which determines the waveform of the ^{57}Co source [66]. The data acquisition can be changed to MCS mode, measurements commence and produce a histogram plot of intensity of counts versus velocity of the ^{57}Co source.

3.4.6 Calibration of Mössbauer spectra

In this study, the method of calibration was to use α -Fe foil at room temperature. The foil is characterized as follows, 99.99% Fe, 0.01% carbon and has a thickness of approximately 12 μm . Its magnetic field values are ~ 32.9 T, with zero isomer shift and quadrupole splitting values. All isomer shifts are determined with respect to the center of the α -Fe spectrum which serves as a reference. Figure 3.12, shows the velocity profile during the single period which resulted in a spectrum being recorded twice in the 512 channels of MCA. This is illustrated in Figure 3.13. The spectrum in Figure 3.13 was folded so that the total number of channels is reduced to 256, thus eliminating statistical noise. The folded α -Fe foil spectrum gives a six-line pattern where the center spectrum is chosen as zero velocity and is used to set the reference point for the isomer shifts measured. The folded spectra for Transmission Mössbauer spectroscopy (TMS) and conversion electron Mössbauer spectroscopy (CEMS) are shown in Figure 3.14.

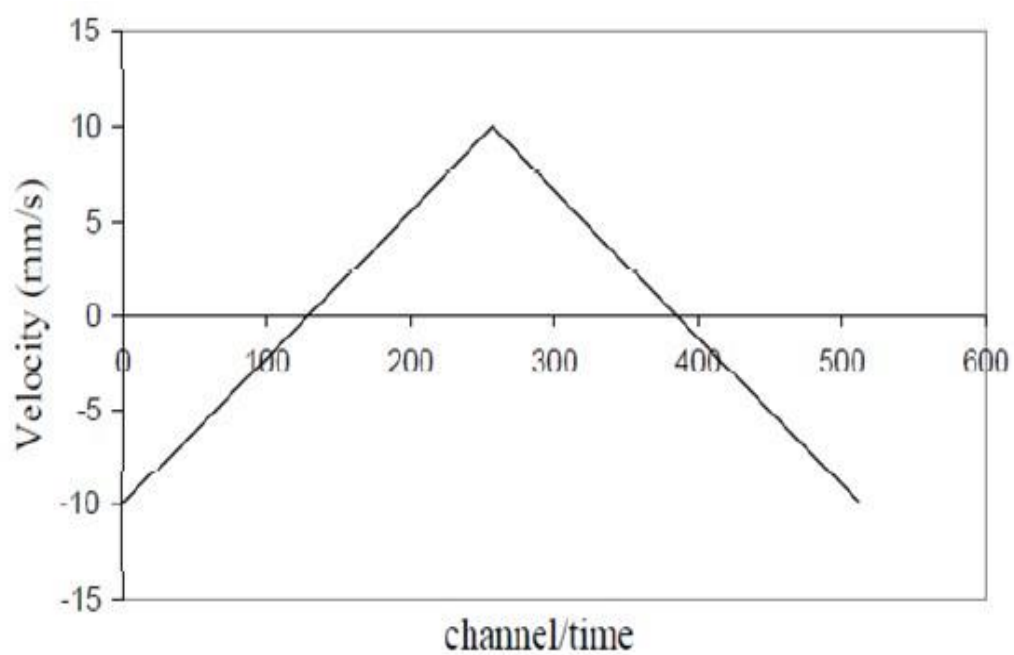


Figure 3.12: Triangular velocity profile as a function of channel number.

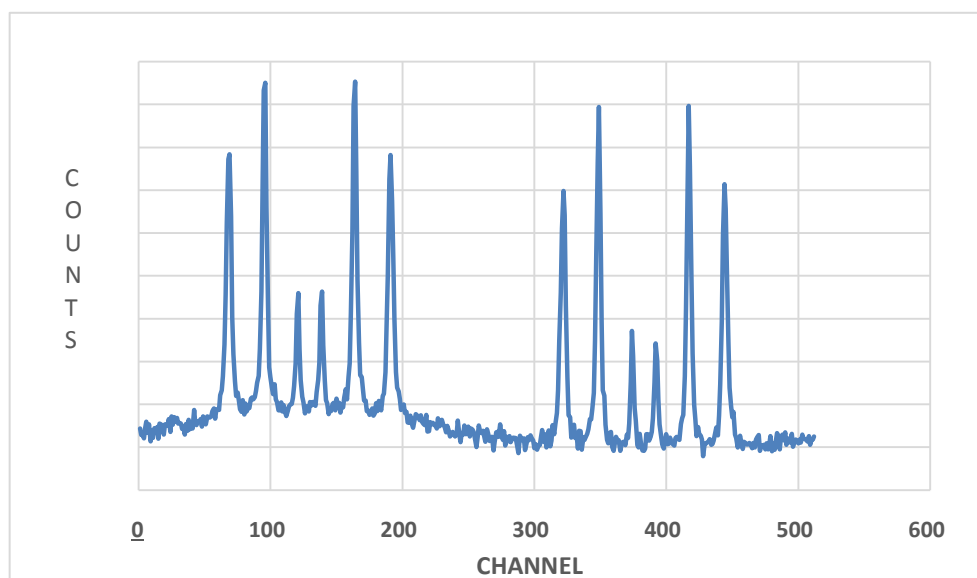


Figure 3.13: Unfolded CEM spectrum of an α -Fe foil.

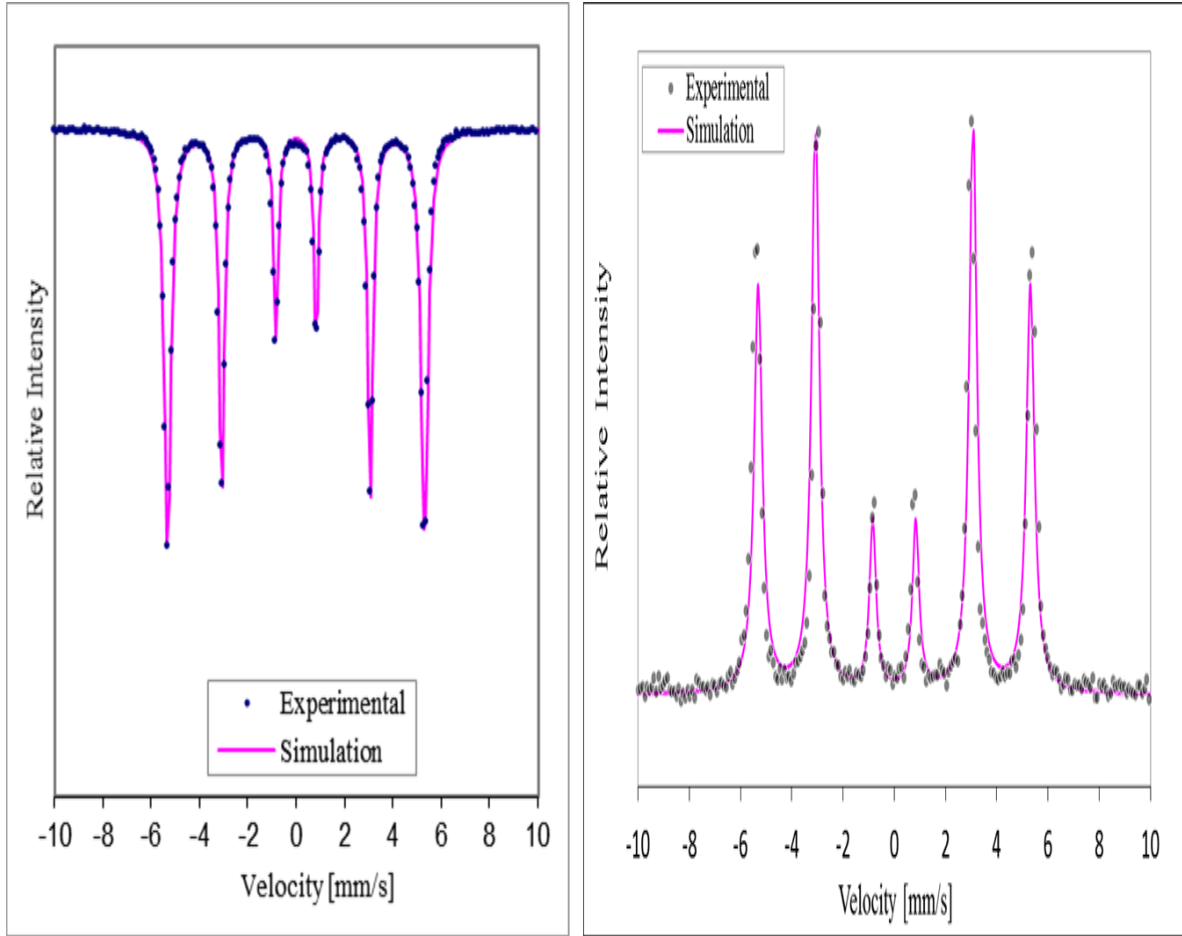


Figure 3.14: Folded Mössbauer spectra for α -Fe in a) Transmission Mössbauer spectroscopy and b) conversion electron Mössbauer spectroscopy measurements (right).

3.4.7 Data analysis

Usually, after the implantation processes, the probe atoms are located on several lattice sites with different hyperfine parameters, resulting in very complex spectra. The analysis involves least-square fitting procedure using Lorentzian lines or voigt line shapes (with Gaussian broadening). The experimental data obtained in this study was analyzed with Mössbauer analysis program RECOIL [67] using Voigt line shapes with a Lorentzian line with Γ (FWHM) = 0.30 mm/s and Gaussian broadening σ .

3.5 Vibrating Sample Magnetometer (VSM)

Magnetic materials are classified into two broad categories, soft and hard [68]. Soft magnetic materials have large permeabilities and very small coercivities (typically less than 1 Oe). While hard magnetic materials are used in permanent magnetic applications and have large saturation, and coercivities (larger than 10 kOe). Whether the materials are hard or soft, characterization of their magnetic properties can best be described in terms of their hysteresis loop. The most common measurement method utilized for hysteresis loop determinations at ambient temperature is the vibrating sample magnetometer (VSM). Invented by Simon Foner, in 1955 at MIT [69]. VSM allows for measurements of magnetic material properties such as hysteresis, saturation magnetization, coercivity, and anisotropy.

In this study, the magnetization measurements were made with a VSM incorporated in a Cryogenics Physical Properties Measurement System (PPMS). A brief description of VSM operation and measurements are discussed below.

3.5.1 Principle of Operation

The VSM is based on Faraday's law which states that an electromagnetic force (emf) is generated in a coil when there is a change in flux through the coil [70]. The principle relies on the detection of the induced emf in a coil wire given by:

$$\varepsilon = -N \frac{d}{dt}(BA \cos \theta), \quad (3.1)$$

where N is the number of turns in a coil, A is the coil turn area, θ is the angle between the applied magnetic field (B) and the direction normal to the coil surface. The operation of VSM is fairly simple. A sample under investigation is placed on a long rod which is driven by a mechanical vibrator. The rod is positioned between the pole pieces of an electromagnet to which detection coils are mounted.

Thus the sample is vibrated at in a vertical direction with respect to the pick-up coils at a fixed frequency. The sample can be magnetized by a horizontal magnetic field generated by an electromagnet. The pick-up coils measure the induced magnetic flux. The resulting variable signal is proportional to the magnetic moment of the material under investigation and also to the vibration frequency and amplitude. The induced signals are fed to a differential amplifier to compensate for variations in amplitude and frequency of oscillations [70-71]. In addition, a lock-in amplifier with phase sensitive detection coupled to a low pass filter generates a direct current output signal that purely depends on the induced magnetic moment from the specimen [42].

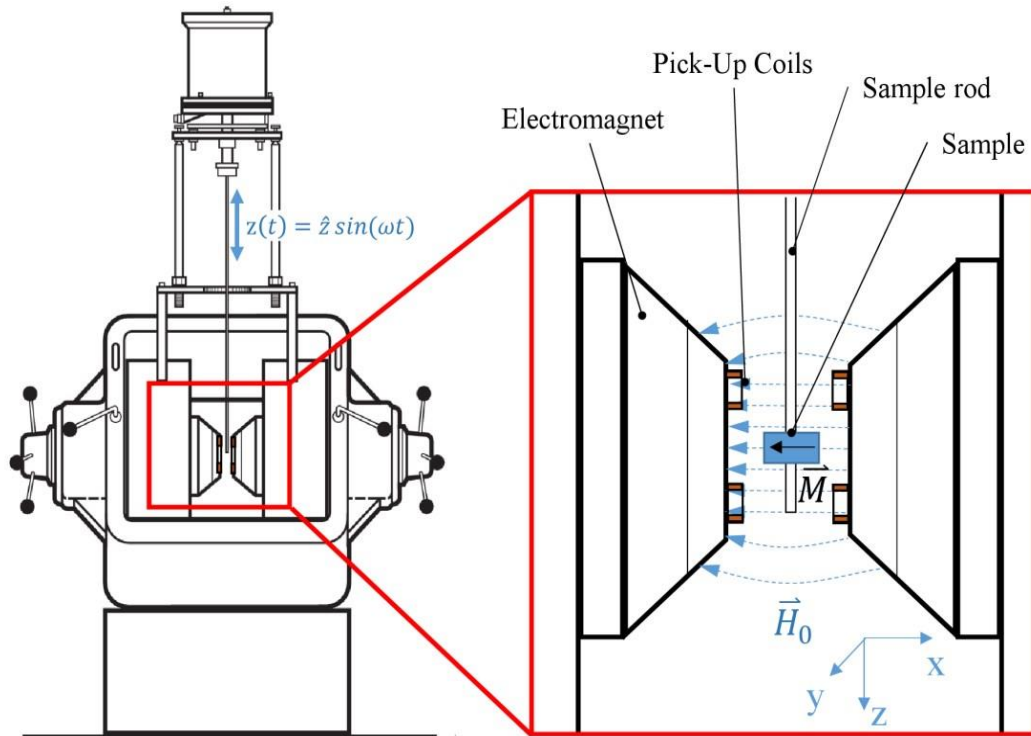


Figure 3.15: Schematic representation of a VSM apparatus. Adapted from [72].

The pick-up coils are matched and connected in opposite sense, such that in the absence of a sample the overall induced voltage is zero. This is because the external magnetic field is induced in equal and opposite directions.

When the sample is in an upward motion, it causes an increase in the flux through the upper pick-up coils and a decrease in the flux through the pickup coils. The reverse is constant with the downward motion of the specimen. As a result, the overall voltage induced when the sample is oscillating is proportional to twice the divergence of the B -field.

3.5.2 VSM measurements

Magnetization curves, $M(H, T_m)$, were measured as a function of measuring temperature (T_m) at 4 K and 293 K after the 1173 K annealing stage. In addition, the magnetization curve of a virgin Al_2O_3 sample was also measured at both measuring temperatures and was used to subtract the diamagnetic background component from the data.

CHAPTER 4

Analysis, Results, and Discussion

This chapter presents the analysis of the data and interpretation of results obtained from the CEMS and VSM measurements on the Fe-implanted Al_2O_3 sample. The first section of this chapter focuses on results from CEMS measurements with special attention given to the structural changes observed in the spectra with annealing increasing temperature. The final section of this chapter focuses on results obtained from VSM measurements.

4.1 CEMS Measurements on Fe-implanted Al_2O_3

The CEMS data was collected with a parallel plate detector operated with acetone gas at a pressure of 35 mbar. The data was collected at room temperature on the as-implanted sample and after annealing the sample for 30 minutes in air at temperatures up to 1173 K.

4.1.1 Analysis and Results

The CEM spectra of the as-implanted and after annealing at temperatures indicated are presented in Figure. 4.1. The as-implanted spectrum is similar to the spectra observed in previous studies on Al_2O_3 implanted with Fe to fluences of 10^{16} - 10^{17} ions/ cm^2 [31,73], showing that the implanted iron ions are in four charge states of Fe^{4+} , Fe^{3+} , Fe^{2+} and Fe^0 , but differ from those observed in other Fe ion implanted Al_2O_3 studies [18,19,28,30,74]. These authors reported that the implanted iron ions are in Fe^{3+} , Fe^{2+} and Fe^0 for an as-implanted samples. The analyses of the spectra in all these studies were conducted in terms of Fe being incorporated in the Al_2O_3 lattice in both Fe^{2+} and Fe^{3+} valence states, which are distinguishable by their distinctly different isomer shift values.

The same procedure was followed in which Mössbauer spectral analysis program RECOIL of Rancourt *et al.*[67], using Voigt lines shapes with a Lorentzian line width Γ (FWHM) = 0.15 mm/s and Gaussian broadening σ were used for the spectral components. Accordingly, the spectrum of the as-implanted sample was fitted with the following components:

- (i) a symmetric doublet D1, with isomer shift $\delta = 1.22(4)$ mm/s, a quadrupole splitting $\Delta E_Q = 1.60(8)$ mm/s, and a large line broadening ($\sigma = 0.50$ mm/s), due to Fe in implantation induced damaged regions/zones in the Al_2O_3 lattice (Fe^{2+});
- (ii) doublet symmetric D2, with $\delta = 0.42(6)$ mm/s and $\Delta E_Q = 1.74(2)$ mm/s, attributed to Fe^{3+} ;
- (iii) doublet symmetric D3, with δ and ΔE_Q values of $-0.08(1)$ and $0.30(1)$ mm/s respectively. This component is attributed to Fe^{4+} and
- (iv) singlet S1, with $\delta = -0.04(6)$ mm/s, attributed to Fe^0 .

A dramatic change in the spectrum is evident, after annealing at 873 K with the inclusion of a doublet component D4 whose parameters are indicative of Fe^{3+} and at temperatures above 1073 K the resonance structure is due to two paramagnetic doublets with isomer shifts characteristic of Fe^{3+} . The parameters extracted from the fits to the spectra are collected in Table 4.1 where the isomer shifts are expressed relative to the centroid of an α -Fe absorber at room temperature (RT). The assignments are based on the information compiled by Gütlich [44].

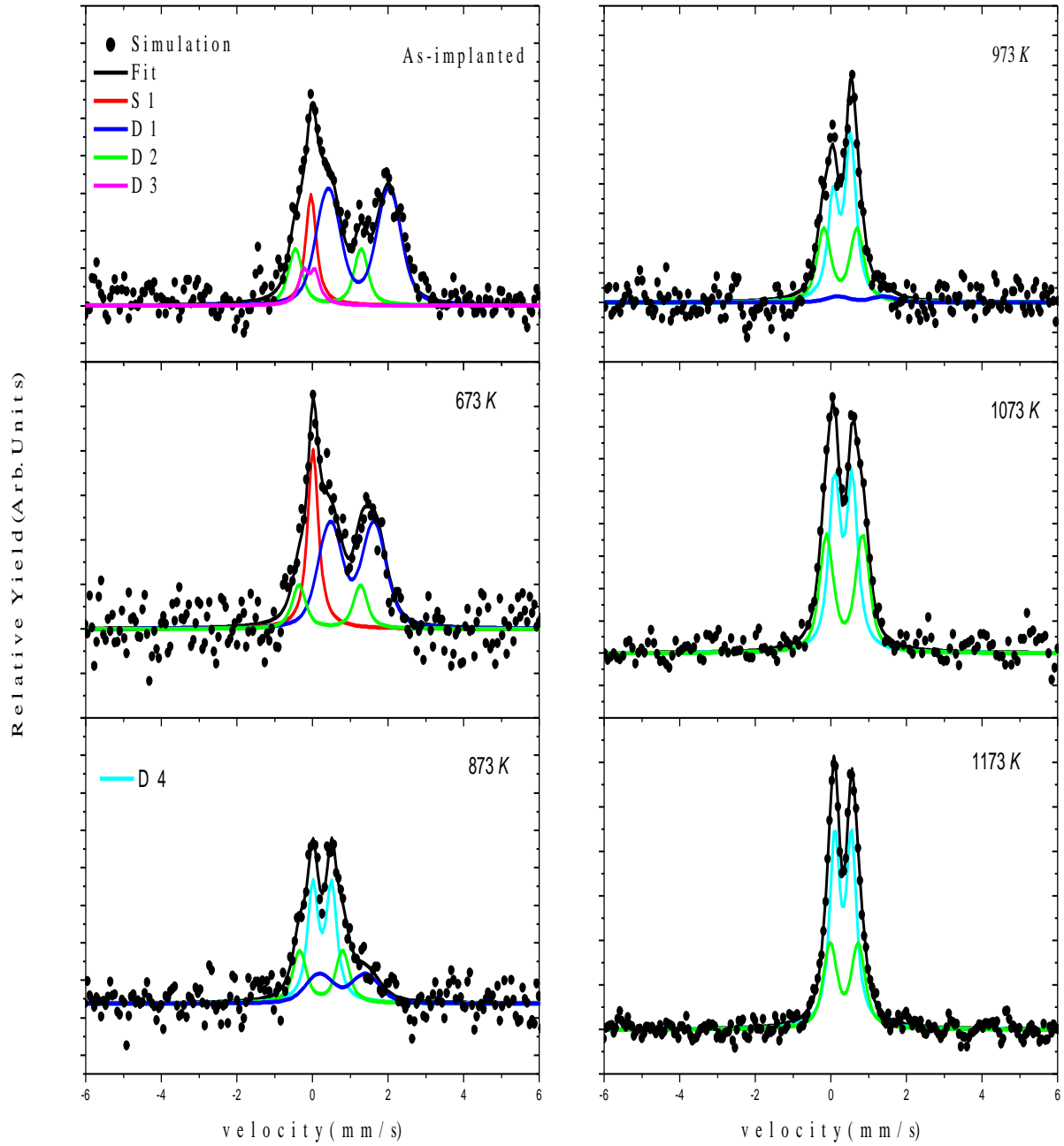


Figure 4.1: CEM spectra of Fe implanted Al_2O_3 collected at room temperature after annealing at the temperatures shown.

Table 4.1: Mössbauer fit parameters, isomer shift (δ), quadrupole splitting (ΔE_Q), area fraction (f_A), and Gaussian broadening (σ) of the spectral components required to fit the CEM spectra.

Annealing Temperature (K)	Component	δ (mm/s)	ΔE_Q (mm/s)	σ (mm/s)	f_A (%)	Assignment
As-implanted	S1	-0.04(6)	0	0.10	15(3)	Fe ⁰
	D1	1.22(4)	1.60(8)	0.50	58(2)	Fe ²⁺
	D2	0.42(6)	1.74(2)	0.20	18(2)	Fe ³⁺
	D3	-0.08(1)	0.30(1)	0.10	8(2)	Fe ⁴⁺
673	S1	0.02(5)	0	0.10	26(2)	Fe ⁰
	D1	1.05(9)	1.16(3)	0.50	58(3)	Fe ²⁺
	D2	0.46(3)	1.63(2)	0.20	15(3)	Fe ³⁺
873	D1	0.79(7)	1.22(5)	0.50	26(3)	Fe ²⁺
	D2	0.23(9)	1.14(1)	0.20	26(3)	Fe ³⁺
	D4	0.26(4)	0.49(7)	0.10	48(2)	Fe ³⁺
973	D1	0.79(7)	1.22(5)	0.50	5(2)	Fe ²⁺
	D2	0.25(5)	0.87(8)	0.20	38(2)	Fe ³⁺
	D4	0.29(3)	0.46(8)	0.10	57(3)	Fe ³⁺
1073	D2	0.36(3)	1.0(1)	0.20	45(2)	Fe ³⁺
	D4	0.33(2)	0.47(8)	0.10	55(2)	Fe ³⁺
1173	D2	0.35(2)	0.74(7)	0.20	36(2)	Fe ³⁺
	D4	0.32(1)	0.44(2)	0.10	64(4)	Fe ³⁺

4.1.2 Spectral parameters and Assignments

4.1.2.1 Spectral component at room temperature

A single line component S1, near zero velocity ($\delta = -0.04(1)$ mm/s) in the spectra can be attributed to metallic iron, Fe^0 . This single line seems to indicate the presence of clusters either as $\alpha\text{-Fe}$ or superparamagnetic $\gamma\text{-Fe}$ [18, 73]. A similar component was observed in other Fe-implanted Al_2O_3 studies [18, 28, 31-32, 73-77].

A symmetric doublet D1 with isomer shift $\delta = 1.22(4)$ mm/s, quadrupole splitting $\Delta E_Q = 1.60(1)$ mm/s, and a large line broadening ($\sigma = 0.50$ mm/s), is due to Fe in implantation induced damaged regions/zones in the Al_2O_3 lattice. This component is assigned to the Fe^{2+} state. Doublet D2, with isomer shift of $0.42(6)$ mm/s and large quadrupole splitting of $1.74(2)$ mm/s is observed throughout the temperature range. This component is attributed to Fe on substitutional Al sites in the lattice (designated Fe^{3+}).

A low intensity doublet D3, with $\delta = -0.08(1)$ mm/s and $\Delta E_Q = 0.30(1)$ mm/s is only observed on the as-implanted sample is attributed to Fe^{4+} ions located in a distorted FeO_6 structure. A similar doublet component was observed with iron implanted Al_2O_3 [76], and iron-implanted polycrystalline Al_2O_3 [28]. The presence of this component in a distorted FeO_6 octahedral environment seems to promote the amorphization of Al_2O_3 . The presence of Fe^{4+} ions in Mössbauer measurements when the sample is implanted with 140 keV ^{57}Fe ions at the fluence of $2.0 \times 10^{17} \text{ cm}^{-2}$, seems to suggest that the implanted layer might be between a vacancy-rich Al_2O_3 lattice and the amorphized layer [28].

4.1.2.2 Annealing Behaviour

Figure 4.2 shows the relative area fractions of the fitted spectral components as a function of annealing temperature in air.

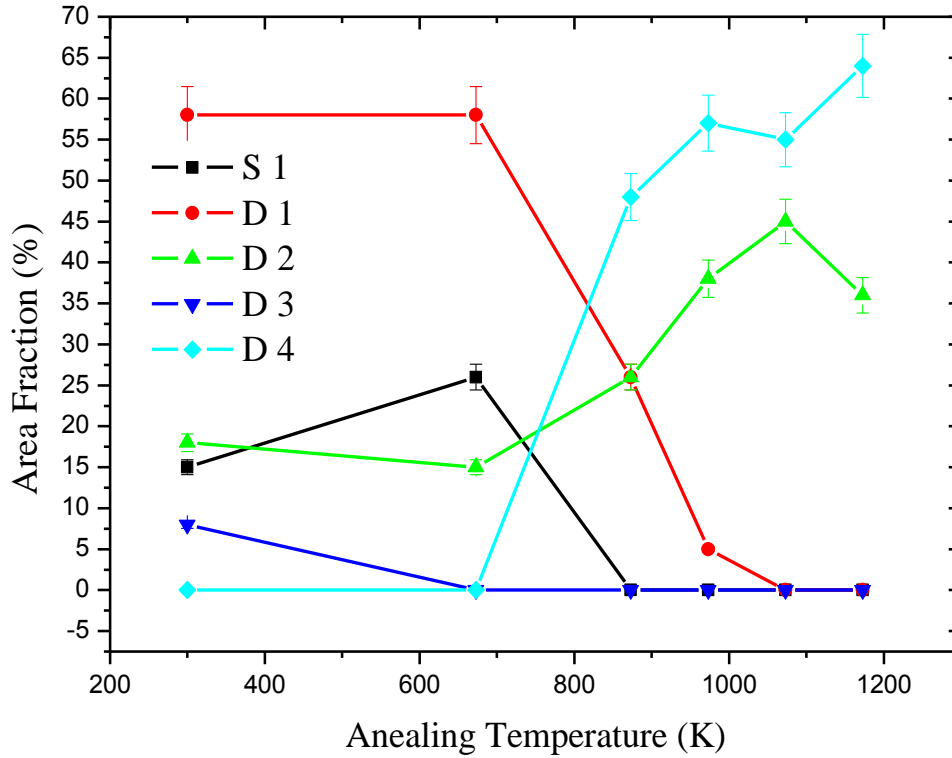


Figure 4.2: Area fraction of components as a function of temperature.

In the temperature range ≤ 673 K, the area fraction of the metallic iron increases from 15(3) % to 26(3) %, with a corresponding decrease in the substitutional Fe area fraction by approximately 3%. The area fraction of the damage site remains fairly constant. Fe^{4+} component completely disappears at 673 K. Donnet *et al.* [73] reported the disappearance of this component after annealing above 673 K in CEMS measurements, resulting a new doublet component whose parameters are characteristic of a mixed oxide containing Fe^{3+} ions and Al^{3+} . Therefore, in this study, we suggest that disappearance of this component at 673 K indicate the transformation of these ions into metal and mixture of oxides containing Fe^{3+} ions.

Annealing of the damage site is evident in the temperature range 673 K – 873 K. The area fraction of the damage site decreased from approximately 58 % at 673 K to

26 % at 873 *K*. In this temperature range, the area fraction of the metallic iron decreases from 26(2) % to 0 % which necessitated the inclusion of a dominant (48(2) %) doublet component with parameters indicative of Fe³⁺ (D4). The increase in the substitutional Fe area fraction from 15(3) % to 26(3) % is attributed to the annealing of the damage site with increasing temperature.

After annealing at temperatures above 973 *K*, the damaged site component disappears completely, indicating that the induced damage is completely annealed. After annealing at 1073 *K* and 1173 *K*, the total amount of implanted iron was oxidized into two paramagnetic doublets (D2 & D4) with isomer shifts that indicative of Fe³⁺ ions. The quadrupole splitting of the component D4 shows little change with annealing, but that of D2 shows a significant decrease, reflecting a reduction in the size dispersion of the clusters. The population of D4 increases at the expense of D2, reflecting an increase in the population of the larger clusters.

4.2 VSM Studies

Magnetization measurements on the Fe-implanted Al₂O₃ sample annealed at 1173 *K* were carried out, using a vibrating sample magnetometer as a function of applied field at temperatures of 293 *K* and 4 *K* at iThemba LABS, Cape Town. The magnetization as a function of the magnetic field are presented in Figures 4.3 (a) and (b). The diamagnetic background due to the substrate was subtracted. The RT magnetization curve displays little evidence of hysteresis. The saturation magnetization M_s is $\sim 8.0 \times 10^{-4}$ emu/g with the coercive field being zero. However, the magnetization curve obtained at 4 *K*. Shown on a smaller range of the applied field in Figure 4.3 (b) shows a small hysteresis effect with a coercive field of ~ 0.05 T providing evidence that at room temperature the magnetic nanoclusters shows superparamagnetic behavior.

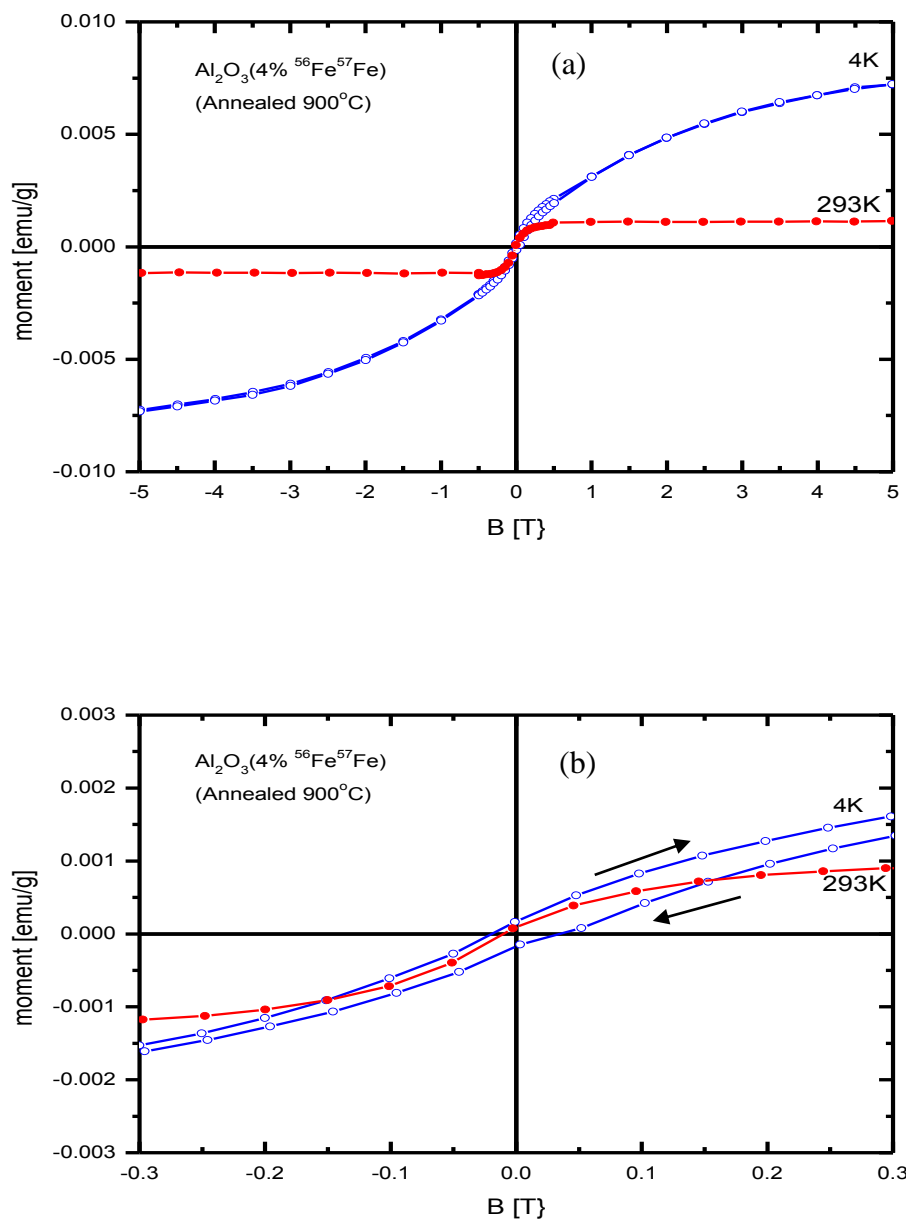


Figure 4.3 (a) & (b): Magnetization curves of $\text{Al}_2\text{O}_3: {}^{57}\text{Fe} + {}^{56}\text{Fe}$ measured at 293 K and 4 K after annealing at 1173 K.

Figure 4.4 presents a plot of moment m , normalized to m_s , as a function of B/T , where B is the applied field and T the measurement temperature. The solid line represents a fit of the Langevin function

$$\frac{m(B,T)}{m_s} = \frac{m_r}{m_s} + \left[\coth\left(\frac{\mu B}{kT}\right) - \frac{kT}{\mu B} \right] + \frac{\chi_b B}{m_s} \quad (4.1)$$

where m_r is a remanent moment at $B = 0$, the term $\chi_b B/m_s$ corrects for contributions from the substrate and μ is the magnetic moment of the particle/cluster.

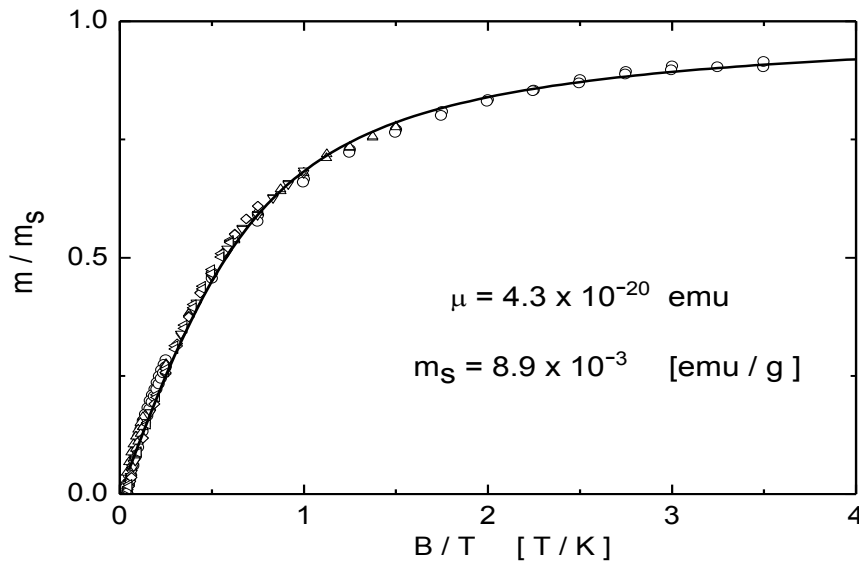


Figure 4.4 The moment m normalized to the saturation moment m_s , plotted as a function of B/T where B is the applied field and T the temperature.

The Langevin function, which is applicable to small magnetic clusters, gives a good fit to the data and confirms the superparamagnetic nature of the Fe clusters. The values for m_s and μ derived from the fitting of the $m(B,T)$ behaviour to the Langevin function allows for the determination of the average volume $V (= \mu/m_s)$ of the clusters.

Analysis of our data yields values $\mu = 4.3 \times 10^{-20}$ emu and $m_s = 8.9(3) \times 10^{-3}$ emu/g, which translate to mean cluster radius of 2-3 nm. Similar sized clusters have been reported for Al₂O₃ implanted with $4\text{-}10 \times 10^{16}$ ions/cm² Fe ions [78].

4.3 Summary of ⁵⁷Fe/⁵⁶Fe implanted in Al₂O₃ results

CEMS measurements were performed on Al₂O₃ single crystal sample implanted with ⁵⁷Fe + ⁵⁶Fe ions to a total concentration of 4 at. %. The CEMS measurements were performed on the as-implanted sample and after annealing the sample at temperatures up to 1173 K. Furthermore, VSM measurements were also carried out at 4 K and 293 K on the sample after the 1173 K annealing.

The CEM spectra showed:

A single line component which disappears after annealing at temperatures ≥ 673 K. This component is assigned to either superparamagnetic α -Fe clusters or to paramagnetic γ -Fe; a symmetric doublet due to radiation damage which dominates the spectra at temperatures ≤ 673 K, which is assigned to Fe²⁺ located in damaged lattice sites because of its isomer shift, large line broadening and quadrupole splitting. This component disappears at temperature ≥ 973 K because the induced damage is completely annealed; a symmetric doublet Fe³⁺ is assigned to Fe on Al substitutional site; an unstable doublet with low intensity assigned to Fe⁴⁺ is present only in the spectrum for the as-implanted sample and; two paramagnetic doublets observed after the 1073 K and 1173 K annealing with isomer shifts that are characteristic of Fe³⁺. This suggest a bi-modal size distribution of the possibly formed clusters upon annealing.

The VSM measurements showed:

The magnetization curve obtained at 4 K, shows a small hysteresis effect with a coercive field of ~ 0.05 T providing evidence that at room temperature behavior magnetic nanoclusters shows superparamagnetic behavior.

CHAPTER 5

Concluding Remarks

CEMS measurements were performed on a single crystal Al_2O_3 sample implanted with concentration of 4 at. % Fe. The results show after radiation damage due to the implantation process had annealed, the spectra consist of two doublets with isomer shifts characteristic of Fe^{3+} . Indicating that Fe ions in Al_2O_3 are complexes clusters of size below the critical size for ferromagnetic behaviour and display superparamagnetic relaxation. With increasing annealing temperature, the quadrupole splittings of the components decrease significantly, suggesting that the cluster increase in size. VSM measurements at RT and 4 K support the CEMS results. Magnetization measurements at RT and at a series of low temperatures down to 2 K, after annealing at 1173 K, confirm the formation of Fe nanoclusters. Analysis of the normalized moment of the cluster in terms of the Langevin function for superparamagnetic particles yields an average cluster radius of 2-3 nm, in good agreement with previous observations.

In an extension of the present study, Bharuth-Ram *et al.* [31] have carried out a detailed magnetization study on the sample at temperatures of 2 K, 4 K, 8 K, 12 K, 16 K and 20 K. The magnetization isotherm, i.e. plot of M/M_s vs B/T , generated from the magnetization vs applied field data, were very well fitted with the Langevin function applicable to small magnetic clusters. The values of the saturation magnetization and the magnetic moment extracted from the fit led to the conclusion that the clusters were 4-6 nm in diameter.

References

- [1] Davis, K. 2010. "Material Review: Alumina (Al_2O_3)", *School of Doctoral Studies (European Union)* : pp.109-114.
- [2] Paglia, G. 2004. Determination of the Structure of α -alumina using empirical and first principle calculations combined with supporting experiments: *in Applied Physics and Applied Chemistry, Curtin University of Technology*.
- [4] Levin, I. and Brandon, D. 1998. "Metastable Alumina Polymorphs: Crystal Structure and Transition Sequences." *J. Am. Ceram. Soc.* **81**, pp. 1995-2012.
- [5] Medvedovski, E. 2002. "Alumina Ceramics for Ballistic Protection." *American Ceramic Society Bulletin* **81(3)**, pp.6.
- [3] Committee, A.I. 1991. "Engineered Material Handbook." *ASM International*.
- [6] Kim, Y. and Hsu, T. 1991. "A reflection Electron Microscopic (REM) study α - Al_2O_3 (0001) Surfaces." *Surface Science*, **258**, pp.131-146.
- [7] Shirai, T., Watanabe, H., Fuji, M. and Takahashi, M. 2007. "Structural Properties and Surface Characteristics on Aluminium oxide Powder." *Materials Chemistry and Physics*, **103**, pp. 394-399.
- [8] CoorsTek. 2006. "CeraShield Armor Ceramics." C.Tek, Editor, Golden, Co.
- [9] http://www.chemicalbook.com/ProductMSDSDetailCB9853056_EN.htm. 2017. Accessed date: 24/04/2017.
- [10] Alsebaie, A.M. 2005. *Characterisation of Alumina-Zirconia Composites Produced by Micro-sized Powders*, MSc Thesis, School of Mechanical and Manufacturing engineering, Dublin City University.

-
- [11] Ishiwa, N., Miyata, T., Minato, I., Marumo, F. and Iwai, S. 1980. "Acta. Crystallogr. Sect. B." *Struct. Crystallogr. Cryst. Chem.*, **36**, pp.228.
 - [12] Vashishta, P., Kalia, R. K., Nakano, A. and Rino, J.P. 2008. "Interaction potentials for alumina and molecular dynamics simulations of amorphous and liquid alumina." *Journal of Applied Physic*, **103**. pp. 083504.
 - [13] Mousavi, S.J. 2013. "Structural and thermodynamics properties of Alumina." *Chemistry of Solid Materials* **1**(2).
 - [14] Vargas, M. and Kioussis, N. 2011. "An ab-initio Examination of the Surface Electronic Structure Alumina α -Al₂O₃(110)." www.csun.edu/~mmv7887/Aluminareport1). Accessed date: 22/03/2017.
 - [15] Touzin, M., *et al.* 2007. "Relationships between the dielectric between resistance and charge transport in Alumina materials-Effects of the microstructure." *Journal of the European Ceramic Society*, **27**, pp.1193-1197.
 - [16] Dlamini, W.B. 2011. *⁵⁷Fe Mössbauer Studies of ⁵⁷Mn* implanted III-V Semiconductors InP and InAs*, MSc Thesis, School of Chemistry and Physics, University of KwaZulu-Natal.
 - [17] Marest, G. 1988. *Surface and Interface Analysis*. **12**: pp.509-518.
 - [18] McHargue C.J., Sklad P.S., McCallum J.C. and White C.W. 1990. "The structure of Al₂O₃ implanted with iron at 77 K." *Nucl. Instr. Methods. Phys. Res.* **B 46**: pp.144 - 148.
 - [19] McHargue, C.J., Farlow, G.C., Sklad, P.S. and White C.W. 1987. "Iron ion implantation effects in Sapphire." *Nuclear Instruments and Methods in Physics Research.* **B (19/20)**: pp. 813-821.
-

-
- [20] McHargue, C.J., Sklad, P.S., White, C.W., Farlow, G.C., Perez, A., and Marest, G. 1991. *J. Mater. Res.* **6**: pp. 2160-2164.
- [21] McHargue, C.J., Sklad, P.S., White, C.W., Farlow, G.C., Perez, A., and Marest, G. 1987. *J. Mater. Res.* **6**. pp. 2145-2150.
- [22] Laurent, C.H., Rousset, A., Vereisi, M., Kanna, K.R., Raju, A.R., and Rao, C.N.R. 1993. *J. Mater. Chem.* **3**: pp. 513-518.
- [23] McHargue, C.T., Ononye, L.C., Alves, E., Marques, C. and Alland, L.F., 2004. *Nucl. Instrum. Meth.* **B 218**: pp. 227-231.
- [24] Hess, J., Levy, A. 1980. "Response of the Mössbauer spectrum of paramagnetic Fe^{3+} in Al_2O_3 to nuclear dipole fields." *Phys. Rev.* **B 22**: pp. 5068-5078.
- [25] Wertheim, G.K., Remeika, J.P. 1964. "Mössbauer effect hyperfine structure of trivalent ^{57}Fe in corundum." *Phys. Lett.* **10**: pp. 14-15.
- [26] Wickman, H.H., Wertheim, G.K. 1966. "Mössbauer hyperfine spectra of Fe^{3+} in corundum: magnetic: and crystal- field effect." *Phys. Rev.* **B 148**: pp. 211–217.
- [27] Donnet, C., Jaffrezic, H., Marest, G., Moncoffre, N. and Tousset, J. 1990. "Iron-implantation sintered alumina studied by RBS, CEMS and SEM techniques. *Nucl. Instr. Meth.* **B 50**: pp. 410-415.
- [28] Guomei W., Shipu L., Ning X., and Donghui F. 1992. "Structure and surface properties of polycrystalline ^{57}Fe -implanted aluminas." *Nucl. Instr. Meth.* **B 72**: pp. 64 - 68.
- [29] Kobayashi, T., Nakanishi, A., Fukumura, K. and Langouche, G. 1998. "Fine iron particles formed in a sapphire crystal by the ion implantation technique." *J. Appl. Phys.* **83**: pp. 4631-4641.
-

-
- [30] Dèzsi, I., Szucs, I. and Fetzer, C.S. 2008. "Iron implantation in α -Al₂O₃." *J. Appl. Phys.* **104**. pp. 034904.
- [31] Bharuth-Ram, K., Doyle, T.B., Adoons, V., Moodley, M.K., and Ronning, C. 2017. "Formation of superparamagnetic nanoclusters in Fe implanted Al₂O₃." *Nuclear Instruments and Methods in Physics Research Section B: Beam Interactions with Materials and Atoms*. Published online: <https://doi.org/10.1016/j.nimb.2017.03.049>.
- [32] Hayashi, N., Sakamoto, I., Wakabayashi, H., Toriyama, T. and Honda, S. 2003. "Formation of nanosized Fe–Co alloys in α -Al₂O₃ crystals by ion implantation." *Journal of Applied Physics*. **94**. pp. 2597.
- [33] McHargue, C.J., Ren, S.X., and Hunn, J.D. 1998. "Nanometer-size dispersions of iron in sapphire prepared by ion implantation and annealing." *Mater. Scie. Eng.* **A253**: pp. 1-7.
- [34] Hayashi N., Toriyama T., Wakabayashi H., Sakamoto I., Okada T., and Kuriyama K. 2002. "Nano-clustering in α -Al₂O₃ crystals by ion implantation of iron and cobalt and their magnetic properties." *Surface and Coatings Technology*. **158-159**: pp. 193-197.
- [35] Perez, A., Treilleux, M., Capra, T., and Griscom, D.L., 2010. *J. Mater. Res.* **2**: pp. 910.
- [36] Mössbauer, R.L. 1961. "Noble Lecture." pp. 584-601.
- [37] Gutlich, P. and Trautwein, A. 1978. "Mössbauer spectroscopy and transition metal chemistry." pp. 9-29.
- [38] Chen, Y. and Yang, D. 2007. *Mössbauer effect in lattice dynamics-experimental techniques and applications*. Weinheim: Willey-VCH.
-

-
- [39] Perez A., Marest G., Sawicka B.D., Sawicki J.A. and Tyliszczak T. 1983. *Phys. Rev. B* **(28)**: pp. 1227.
- [40] Masenda, H. 2014. *Are Fe and Co implanted ZnO and III-nitride semiconductors magnetic?*. PhD Thesis. School of Physics, University of Witwatersrand.
- [41] Lin, C.M., and Lin, S.T. 1993. *J. Phys. Condens. Matter.* **5**. pp. L247 - L250.
- [42] Masenda, H. 2010. *^{57}Fe Mössbauer investigations in GaAs and GaP following implantation of $^{57}\text{Mn}^*$* . MSc Thesis. School of Physics, University of Witwatersrand.
- [43] Nordstrom, E. 2001. *Functional Materials Studied by Mössbauer Spectroscopy*. PhD Thesis. Faculty of Science and Technology, University of Uppsala. Sweden.
- [44] Gutlich, P., Bill, E. and Trautwein A. 2011. *Mössbauer Spectroscopy and Transitional Metal Chemistry*. Springer-Verlag.
- [45] Brent, F. 2011. *Mössbauer spectrometry in characterization of materials*. New York: John Wiley.
- [46] Molholt, T.E. 2012. *Paramagnetism in ion-implanted oxides*. PhD Thesis. Faculty of Physical Sciences, University of Iceland.
- [47] Ibwanga, M. 2016. *A spectroscopy study of Fe phases in cemented carbides*. MSc Thesis. School of Physics. University of Witwatersrand.
- [48] Kalska-szostko, B. 2000. *Mössbauer Spectroscopy on Selected Magnetic Compounds*. PhD Thesis. Faculty of Science and Technology. Uppsala University. Sweden.
-

-
- [49] Langouche, G. 1989. "Ion Implantation in Semiconductors Studied by Mössbauer spectroscopy." *Hyperfine Interactions*. **45**. pp. 199-216.
- [50] White, C.W., McHargue, C.J., Sklad, P.S., Boatner, L.A. and Farlow, G.C. 1986; 60. "Ion implantation and annealing of crystalline oxides." *Mater. Res. Soc. Symp. Proc.* pp. 337-344.
- [51] White, C.W., Boatner, L.A., Sklad, C.J., McHargue, C.J., Rankin, J. and Aziz, M.J. 1988. "Ion implantation and annealing of crystalline oxides and ceramic materials." *Nucl. Instr. Meth.* **B 32**. pp. 11-22.
- [52] Ziegler, J.F.: Ion implantation Physics. 1992. In Ziegler J.F., ed., *Handbook of Ion implantation Technology*. North Holland.
- [53] Gunther, W.K. 1964. *Mössbauer Effect: Principles and Applications*. New York and London: Academic Press.
- [54] Gütlich, P., 2007. Mössbauer spectroscopy principles and applications, Lecture Notes, University of Mainz. pp. 37-52.
- [55] Langouche, G. and Yoshida, Y.: Ion Implantation. 2013. in Yoshida, Y. and Langouche, G., eds., *Mössbauer Spectroscopy*. Berlin Heidelberg: Springer-Verlag.
- [56] Rubin, L. and Poate, J. 2003. *American Institute of Physics*. **9**. pp. 12-15.
- [57] Mayer, J.W., Eriksson, L. and Davies, J.A., eds. 1970. *Ion Implantation in Semiconductors*. New York: Academic Press.
- [58] Crowder, B.L., ed. 1973. *Ion Implantation of Semiconductors and other Materials*. New York: Plenum Press.
-

-
- [59] Chernov, F., Borders, J.A. and Brice, D.K., eds. 1976. *Ion Implantation in Semiconductors*. New York: Plenum Press.
- [60] Hirvonen, J.K., eds. 1980. *Treatise on Material Science and Technology, Vol. 18. Ion Implantation*. New York: Academic Press.
- [61] Picroux, S.T. and Choyke, W.J., eds. 1982. *Metastable Materials, Formation by Ion Implantation*. Amsterdam: North-Holland.
- [62] Ziegler, F.J. and Biersack, J.P.: “James Ziegler - SRIM & TRIM.” <http://www.srim.org>.
- [63] Gonser, U. 1981. In *Mössbauer spectroscopy II (The Exotic side of the method)*. Springer, Germany, pp. 140-149.
- [64] Moodley, K.M. 1999. *The Construction of a CEMS detector and its application to the study of Fe-silicides*. MSc Thesis. Department of Physics. University of Durban-Westville.
- [65] Weyer, G., 1976. *Application of Parallel-Plate Avalanche Counters in Mössbauer spectroscopy*. in I.J. Gruvermand and C.W. Seidel, "Mossbauer effect Methodology". New York and London: Plenum Press.
- [66] Vertes, A., Nagy, S., Klencsar, Z., Lovas, G. and Rosch, F. 2011. *Handbook of Nuclear Chemistry*. Springer Science + Business.
- [67] Rancourt, D.G. 1989. *Nuclear Instruments and Methods in Physics Research*. **B 44**. pp. 199-210.
- [68] Dodrill. N.D. *Measurements with a VSM*. Lake Shore Cryotronic, Inc, www.lakeshore.com. Accessed date: 13/03/2017.
-

-
- [69] Foner, S. 1959. "Versatile and Sensitive Vibrating -Sample Magnetometer." *Rev. Sci. Instrum.* **30**. pp. 548-557.
- [70] Burgei, W., Pechan, M.J. and Jaeger, H. 2003. "A simple vibrating sample magnetometer for use in a materials physics course." *Am. J. Phys.* **71** (8). pp. 825-828.
- [71] Dyar, M.D., Agresti, D.G., Schaefer, M.W., Grant, C.A. and Sklute, E.C. 2006. "Mössbauer Spectroscopy of Earth and Planetary Materials." *Annu. Rev. Earth Planet. Sci.* **34**. pp. 83.
- [72] Lake Shore cryotronics, Inc, *User's Manual 7300 Series vsm system*.
<http://www.lakeshore.com/ObsoleteAndResearchDocs/7300Manual.pdf.2003>.
Accessed date: 13/03/2017.
- [73] Donnect C., Jaffrezic H., Marest G., Moncoffre N., Tousset J. 1990. "Iron-implanted sintered alumina studied by RBS, CEMS, and SEM techniques." *Nucl. Instr. Meth. Phys. Res.* **B 50**. pp. 410 - 415.
- [74] Sakamoto, I., Honda, S., Tanoue, H., Hayashi, N. and Yamane, H. 1999. "Structural and Magnetic properties of Fe ion implnated Al₂O₃." *Nucl. Instr. Meth. Phys. Res.* **B**. pp. 1039-1043.
- [75] Gütlich, P., Bill, E. Trautwein, A. 2011. *Mössbauer spectroscopy and Transition metal, Fundamental and Application*, Springer-Verlag. pp. 85.
- [76] Hayashi N., Sakamoto I., Tanoue H., Wakabayashi H. 2002. "Iron clustering and the magnetic properties in α -Al₂O₃ crystals after iron implantation to high doses." *Hyperfine Interactions*. (141/142): pp. 163-168.
-

-
- [77] Kinoshita R., Sakamoto I., Hayashi N., Nomura K., Honda S., Ishida T., Lio S., Tashiro H., and Toriyama T. 2011. "Structural and magnetic properties of Fe and Au ion - implanted Al_2O_3 single crystals." *Japanese Journal of Applied Physics*. **50**. pp. 01BE01.
- [78] McHargue C.J., Ren S.X. and Hunn, J.D., 1998. *Mater. Sci & Eng.* **A253**, pp.1-7.